

AUTOMATED MOTION CONTROL OF A GROUND-VIEWING RADIOMETER SYSTEM

by

Jay Hankerson

Copyright © Jay Hankerson 2018

A Thesis Submitted to the Faculty of the

COLLEGE OF OPTICAL SCIENCES

In Partial Fulfillment of the Requirements

For the Degree of

MASTER OF SCIENCE

In the Graduate College

THE UNIVERSITY OF ARIZONA

2018

THE UNIVERSITY OF ARIZONA
GRADUATE COLLEGE

As members of the Master's Committee, we certify that we have read the thesis prepared by **Jay Hankerson**, titled **Automated Motion Control of a Ground-Viewing Radiometer System** and recommend that it be accepted as fulfilling the thesis requirement for the Master's Degree.



Jeff Czaplak-Myers

Date: 26 Nov 2018




John Koshel

Date: 11/21/2018




Dae Wook Kim

Date: 11/20/18

Final approval and acceptance of this thesis is contingent upon the candidate's submission of the final copies of the thesis to the Graduate College. 

I hereby certify that I have read this thesis prepared under my direction and recommend that it be accepted as fulfilling the Master's requirement.



Jeff Czaplak-Myers
Associate Research Professor of Optical Sciences
Optical Sciences

Date: 26 Nov 2018

Acknowledgements

I thank my advisor, Jeff Czapla-Myers, for his support and guidance throughout my thesis work and studies at the University of Arizona. I also thank RSG member Nik Anderson for his guidance and comments concerning this thesis, and committee members John Koshel and Dae Wook Kim for their valuable input.

Table of Contents

List of Figures	6
List of Tables	8
Abstract	9
Chapter 1: Introduction	10
1.1 Overview of Thesis	10
1.2 Ground-based Satellite Radiometric Calibration	11
1.3 Railroad Valley, Nevada (RRV)	14
Chapter 2: Instrumentation	17
2.1 GVR Design	17
2.2 Laboratory Radiometric Calibration	20
2.3 Application of Spectral Band Adjustment Factors	21
Chapter 3: Field Measurements	26
3.1 Data Acquisition	26
3.2 Data Processing	29
3.3 Results	30
Chapter 4: GVR Translation Stage Design	36
4.1 System Requirements	36
4.2 Translation Stage Design	37
4.3 Motor Considerations	41
4.4 Translation Stage Electronics	43
Chapter 5: Conclusion and Future Work	44
5.1 Conclusion	45
5.2 Future Work	45
Appendix A: Reflectance Analysis from Field Campaign Jul–Aug 2017	47
A.1 31 Jul 2017	48
A.2 1 Aug 2017: Collection 1	49
A.3 1 Aug 2017: Collection 2	50
A.4 2 Aug 2017	51
Appendix B: Ball Screw to Motor Shaft Parallel Error	52
Appendix C: Custom Parts	53
C.1 Adjustor Handle 1	54
C.2 Adjustor Handle 2	57
C.3 Tripod Shaft to Adjuster Handle Mount	58
C.4 Clamp 1 for Bearing. Qty. 2	59
C.5 Clamp 2 for Bearing	60
C.6 Clamp 3 for Bearing	61
C.7 GVR Mount Plate	62

Table of Contents—Continued

C.8	Motor Mount Plate.....	63
C.9	Ball Nut Bracket	65
C.10	Modified Ball Screw	66
	References.....	67

List of Figures

Figure 1.1. RSG member retrieving reflectance data using an ASD at RRV on 5 Jul 2004.	12
Figure 1.2. Sentinel-2A image of RRV taken 2 Mar 2017. The blue square represents a 1km x 1km area at the location of RadCaTS.	15
Figure 1.3. GVR stationed at RadCaTS in RRV, Nevada. Note the cracks in the playa.....	16
Figure 2.1. Single GVR module assembly.....	17
Figure 2.2. Inside of a GVR head. The eight cylinders are the modules and in the middle are the signal electronics. On the other side of the aluminum base is the hot side of the TE cooler, heat sink, and cooling fan (hidden).....	19
Figure 2.3. GVR head (left) and ASD (right) viewing an SIS during the radiometric calibration of the GVR.	21
Figure 2.4. Relative spectral response of GVR 24, which is currently deployed in RRV, and CaTSSITTR, which is the transfer radiometer used for cross-calibration. The bands shown have center wavelengths in nm of 400, 450, 500, 550, 650, 850, and 1000.	23
Figure 3.1. ASD setup at Railroad Valley. The foreoptic is mounted on the aluminum arm on the tripod. The signal electronics are on the table under the laptop and the laptop stored the data taken. Fiber optic runs from the foreoptic to the electronics.	27
Figure 3.2. Spectral reflectance calculated from data taken by an ASD on 2 Aug 2017. Every 5 cm a new data set is retrieved. At most, there is a difference in reflectance of roughly 0.11.	30
Figure 3.3. Average reflectance on 2 August round 1 as measured by the ASD. The solid line is the average reflectance over 91 cm and the dashed lines are the standard deviation.	31
Figure 3.4. Top view of the arm, tripod, and foreoptic of the ASD spectroradiometer. The ground has cracks, holes, and bumps that affect the spatial uniformity of the area. Photo taken 31 Jul 2017.....	32
Figure 3.5. Reflectance of RRV by the center bandwidth of each channel on a GVR. Data retrieved using an ASD on 2 Aug 2017 round 1.....	33
Figure 3.6. Cumulative average reflectance as the ASD translates on the ground. A data set, n , is taken every 5 cm.	34
Figure 4.1. Basic design of GVR translation stage. The two support shafts and ball screw are suspended between two posts. A motor drives the ball screw, which drives the linear motion of the GVR.....	37
Figure 4.2. SolidWorks model of a GVR mounted on the translation stage. Each tripod has had one leg removed to ensure the GVR has a clear view of the ground. The vertical posts are lower than the legs because they will be inserted into the ground for stability.	38
Figure 4.3. Close-up of GVR mounts. The GVR is mounted to two linear bearings that ride on the support shafts. In the center of the shafts is the ball screw, which drives the ball nut that is attached to the GVR as well. Not shown: cables and corresponding protective carriers..	39

List of Figures—Continued

- Figure 4.4. Two custom parts define the orientation of the support shafts and ball screw. Left is the view from the exterior of the system and the right is the reverse. The square plate on the right has an arc slot that allows for angle adjustments. Not shown are the necessary fasteners for assembly..... 40
- Figure 4.5. Cable carrier providing protection and support for the GVR cables. The carrier is supported by a trough. Not shown are the various cables from the GVR. 44

List of Tables

Table 2.1 Effects of applying SBAFs to GVR 24 (deployed at RadCaTS) to match CaTSSITTR via ASD spectroradiometer reflectance data.....	25
Table 3.1. Summary of the conditions and challenges of each reflectance data set collected.....	29
Table 3.2. Distance the ASD has translated where $R \leq 0.02$	35
Table 4.1. Estimates of torque required due to acceleration for a changing time of acceleration.	42

Abstract

The Remote Sensing Group (RSG) at the College of Optical Sciences of the University of Arizona implements a reflectance-based approach for vicariously calibrating remote sensors. This includes the automated radiometric data collection of the surface of Railroad Valley, Nevada (RRV) using four stationary Ground-Viewing Radiometers (GVRs). There are features such as cracks, pits, and small mounds on the surface of RRV. The ground instantaneous field-of-view (GIFOV) of a stationary GVR may contain more or less of these features than is indicative of the entire site. This thesis presents a design to increasing the spatial sampling via an automated motion control system that will translate the GVR over RRV a short distance. This will make for more accurate data collection in the automated reflectance-based calibration approach.

Chapter 1: Introduction

1.1 Overview of Thesis

This thesis describes improvements to the ground-based radiometric calibration system that the Remote Sensing Group (RSG) of the College of Optical Sciences at the University of Arizona operates at Railroad Valley, Nevada (RRV). Chapter 1 introduces the current instruments and methods used at RSG's radiometric calibration test site. This includes the data collection, atmospheric characterization, and radiative transfer code used for the ground-based radiometric calibration of Earth-observing sensors. The optical, spatial, spectral, and temporal qualities of RRV, as well as the description of the radiometric calibration test site are also presented in Chapter 1.

Chapter 2 describes the ground viewing radiometers (GVRs) that are used to measure the radiance reflected from the test site surface. This, in turn, is used to determine the surface reflectance at each GVR for a given time of interest. A review of the GVR design, including the detector, optics, cooling system, power system, and laboratory radiometric calibration is presented. The spectral band adjustment factor (SBAF), which is used to improve the accuracy in the cross-calibration between sensors, is also described in this chapter.

Chapter 3 describes the field measurement techniques used for this thesis. It covers the data collection process, RRV conditions during data retrieval, data processing, and the results. The results include the average reflectance over time, the reflectance by wavelength, a cumulative average approach to reflectance, and SBAF calculations.

The design of the GVR translation stage is discussed in Chapter 4. This includes a mechanical overview of the various components used and the mechanical analysis for the critical

factors driving the design. It describes the power supply, motor driver and controller, and control software.

Chapter 5 concludes the thesis with a discussion of the conclusions, and future work. It also includes recommendation for the installation of the automated motion control system on a GVR to be used at RRV.

1.2 Ground-based Satellite Radiometric Calibration

There are two phases that Earth-observing sensors are calibrated: pre-launch and post-launch. Vicarious calibration is one post-launch technique that refers to any method that does not rely on on-board calibration systems. RSG utilizes a vicarious ground-based satellite radiometric calibration method that requires the surface reflectance and atmospheric characteristics be used as inputs into a radiative transfer code that is then used to determine the at-sensor spectral radiance, which is then compared to the sensor under test (1).

The traditional reflectance-based approach involves a commercially available spectroradiometer that is used to collect surface-reflectance at RRV at the same time as a sensor passes over the site. The Analytical Spectral Devices (ASD) spectroradiometer covers the visible



Figure 1.1. RSG member retrieving reflectance data using an ASD at RRV on 5 Jul 2004.

and near-infrared (VNIR) portion of the spectrum (350-1050 nm) and the shortwave infrared (SWIR) portion (1050-2500 nm). The ASD is equipped with a silicon array for the VNIR and two indium-gallium-arsenide (InGaAs) detectors for the SWIR. The ground is observed by the ASD via an 8° field of view foreoptic at the end of an optical fiber. The foreoptic is attached to the end of a boom arm that is held away from the user during data collection to avoid the user's shadow. The ASD is carried around a predetermined path while continuously taking data. Data are also retrieved periodically from a reference panel of known reflectance, which is used to compare the

digital numbers of ground vs. the panel. Digital numbers of the ground are then converted to reflectance (2). The equation used for the surface BRF, ρ , is

$$\rho_{ground} = \rho_{panel} \frac{DN_{ground}}{DN_{panel}} \quad (1.1)$$

where ρ_{panel} is the reflectance of the reference panel [unitless], DN_{ground} is the digital number recorded by the ASD while viewing the ground, and DN_{panel} is the digital number recorded by the ASD while viewing the reference panel (3).

Atmospheric characterization data are taken simultaneously to the surface reflectance data retrieval. The 10-channel automated solar radiometer (ASR) is the primary instrument used for atmospheric measurement. The ASR tracks the sun and measures the incoming solar irradiance extinction due to atmospheric absorption and scattering. The data are then utilized to determine the atmospheric transmission and radiance for each of the bands.

RSG has transitioned to an automated approach to ground-based vicarious calibration. Four nadir-viewing radiometers are used to retrieve the surface bidirectional reflectance factor (BRF) of RRV. The BRF, ρ , from the radiometers is determined by

$$\rho = \frac{\pi CV}{E_o \tau_{direct} \cos \theta + E_{sky}} \quad (1.2)$$

where C is the calibration coefficient of the radiometer, V is the voltage of the radiometer, E_o is the exoatmospheric irradiance, τ_{direct} is the atmospheric transmission of the direct solar beam, θ is the solar zenith angle, and E_{sky} is the diffuse sky irradiance. E_o , τ_{direct} , and E_{sky} are determined using data collected by the automated Cimel 318 Sun photometer at RRV. A spherical integrating sphere and a NIST-traceable transfer radiometer are used to determine C for each channel of each GVR. Total ozone mapping spectrometer data supplies the ozone amount over the site for the

desired date. A meteorological station at RRV supplies the atmospheric conditions such as pressure and temperature (3).

The Ground Viewing Radiometers (GVRs) have been absolutely radiometrically calibrated in contrast to the ASD surface measurements, where a reference panel is used. However, reflectance is calculated from the GVR data, as shown in equation 2, as it is from the ASD data. The design of the GVRs are discussed in the instrumentation section of this thesis.

The reflectance data and atmospheric data are inputs to the MODerate resolution atmospheric TRANsmission (MODTRAN) radiative transfer code. MODTRAN is used to predict the top-of-atmosphere (TOA) band-averaged spectral radiance for a given time of interest (4).

1.3 Railroad Valley, Nevada (RRV)

Railroad Valley has been used by the RSG of the University of Arizona since 1996 as a site for the vicarious calibration of airborne and satellite sensors. These include such sensors as Advanced Spaceborne Thermal Emission and Reflection Radiometer (ASTER) (6), Landsat-5 Thematic Mapper (TM) (1), Landsat-7 Enhanced Thematic Mapper Plus (ETM+) (7), Landsat-8 Operational Land Imager (OLI) (5), and the Moderate Resolution Imaging Spectroradiometer (MODIS) onboard the Terra and Aqua platforms (8).

RRV is a dry lake bed, or playa, approximately 500 km north of Las Vegas, Nevada and 160 km east of Tonopah, Nevada. The playa is approximately 10 x 15 km and at an elevation of 1430 m. The Radiometric Calibration Test Site (RadCaTS) is the location where the GVRs are deployed within RRV. The location for RadCaTS was determined by proximity to the access road and that the BRF of the area was indicative of the entirety of RRV (3). RRV is used as the calibration site for practical reasons such as accessibility via roads and proximity to Tucson, AZ. It is also chosen for the optical qualities of the site. Images from Landsat TM, SPOT (Satellite

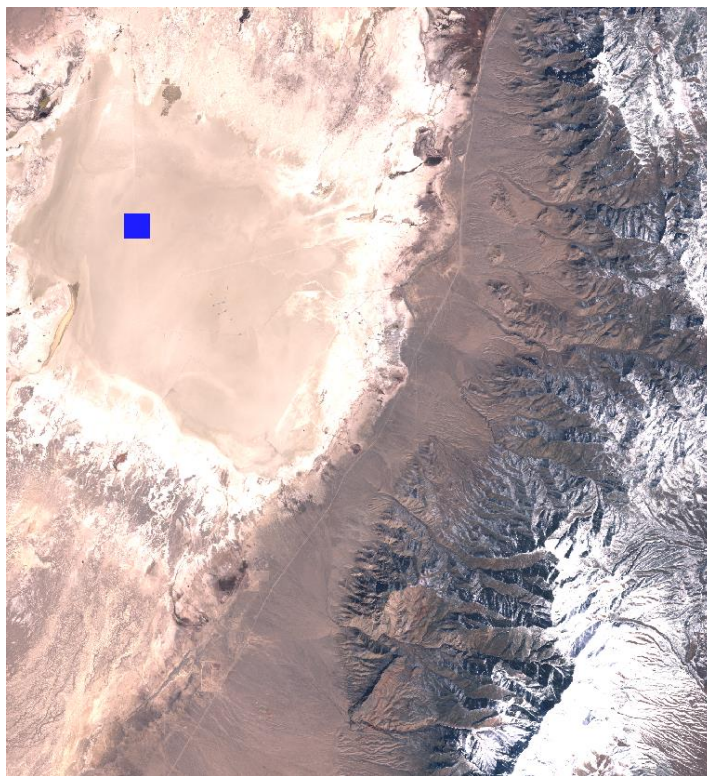


Figure 1.2. Sentinel-2A image of RRV taken 2 Mar 2017. The blue square represents a 1km x 1km area at the location of RadCaTS.

Pour l'Observation de la Terre) HRV (High Resolution Visible), and AVHRR (Advanced Very High Resolution Radiometer) were gathered to analyze certain optical characteristics of RRV. For all the bands of SPOT, and the first four bands of Landsat TM, multiple sites within RRV are found to be spatially uniform at the $\pm 1.5\%$ level over 2×2 km area and $\pm 2.5\%$ over 3×3 km sites under

stable conditions. Surface reflectance is relatively high at 0.3, and is spectrally flat, from 0.6–2.0 μm (9). The large area and high elevation of RRV minimizes the effects of scattered light from outside of the target area and reduces uncertainty due to aerosols, respectively.

Since the four GVRs implemented at RRV are stationary, the data consists of four points averaged to return the reflectance of the playa. The dirt that makes the playa floor has features that are plainly visible at GVR heights, but not visible to satellite sensors that have a ground instantaneous field-of-view (GIFOV) on the order of tens of meters. As shown in Figure 1.3, there are cracks in the playa that form when it dries from rain. A stationary GVR may have more or less cracks in its GIFOV than is indicative of the entire site. Translating the GVR over the ground will allow for data that are more indicative of the site by increasing the spatial sampling. This is the motivation behind this thesis, which describes a method to improve the spatial sampling of the site.



Figure 1.3. GVR stationed at RadCaTS in RRV, Nevada. Note the cracks in the playa.

Chapter 2: Instrumentation

2.1 GVR Design

Each GVR has eight detectors housed in a single radiometer: seven silicon and one InGaAs. There are eight individual detector modules that consist of a front aperture, bandpass filter, rear aperture, detector, and baseplate. The bandpass filter is approximately 20 nm FWHM and located in front of the rear aperture for spectral selection. Seven of the channels are in the VNIR (400, 450, 500, 550, 650, 850, 1000 nm), and one is in the SWIR (1550 nm). The 10° full field of view (FFOV) of each detector module is fully limited by the two apertures. Figure 2.1 shows an exploded view of a single detector module. The GVR detector plane is situated 1.5 m above the

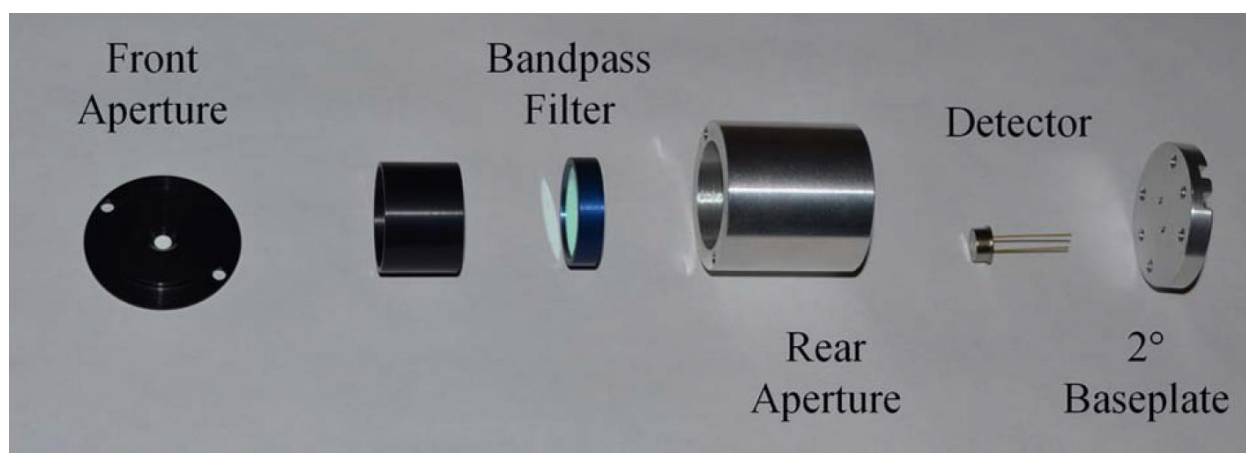


Figure 2.1. Single GVR module assembly.

ground when the instrument is fully deployed, which translates to spot size diameter of 26.2 cm for each detector. The detector baseplate has a 2° angle. This is so that all eight modules view the same location on the ground when the GVR is positioned at the specified height. The modules are oriented in a circular pattern, with the 2° angle pointing toward the centerline of the device. When the detector plane is 1.5 m above the ground, each module views the same spot on the ground. This allows for the spatial variations on the ground to have minimal effect on the data collected between

detectors while having viewing angles close to nadir (10) (11). The angle of the modules do not adversely affect radiometric data collected because BRDF values are consistent at near-nadir viewing angles as shown by previous work (12).

The GVRs are equipped with a thermoelectric (TE) cooler, which is necessary to maximize the stability and accuracy of the instrument. The TE cooler stabilizes the temperature of the critical optical and electronic components to minimize the band-dependent temperature variations. The GVR head consists of two sections. The lower section contains all the detectors and corresponding modules as well as the signal electronics, mounted to a temperature-controlled aluminum plate. The upper section contains the hot side of the TE cooler, which consists of a heat sink and cooling fan.

The cold side of the 12-V, 36-W cold plate TE cooler system is in direct contact with the detectors and detector modules. This allows for increased thermal control on the most critical parts versus an air cooler system. A bi-directional temperature controller set to 25°C controls the system. There is a thermistor mounted near a detector, which is logged as temperature feedback that is independent from the TE cooler.

The TE cooler is power intensive, so logic in the data logger toggles a solid-state relay to turn on the TE cooler based on certain logged events. When the voltage signal from the 850-nm channel reaches the threshold, the TE cooler is switched on. This means that temperature control only occurs when there is adequate signal; cooling will not occur during the night, or during excessively cloudy conditions. This procedure reduces the power that the cooler uses, which is important in a solar-powered field-deployable system.

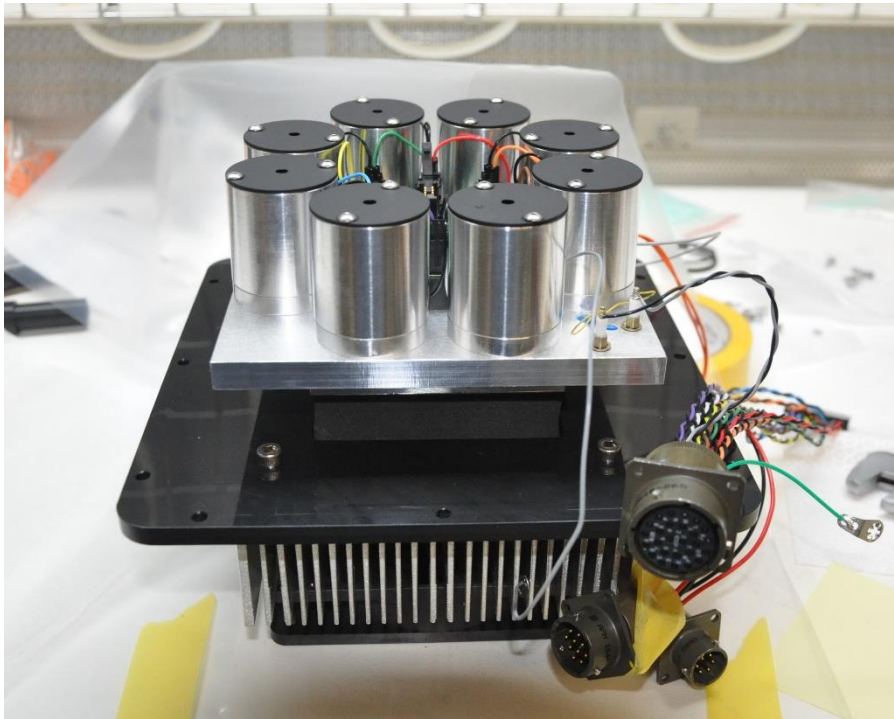


Figure 2.2. Inside of a GVR head. The eight cylinders are the modules and in the middle are the signal electronics. On the other side of the aluminum base is the hot side of the TE cooler, heat sink, and cooling fan (hidden).

Each GVR is powered by a 40-Ah battery and solar-charging system. A 190-W solar panel at each GVR is capable of charging the battery when it is near depletion in one day in fair solar conditions. A maximum power point tracking (MPPT) solar charger controls the solar charging, battery, and general load circuit. It can supply a maximum of 15 A to the load and/or battery. A noise-reduction circuit is built into the load output side which is necessary, because the MPPT outputs voltage with a large (measured at roughly 3 V peak-to-peak), high-frequency noise (11). The noise-filtered power supplies three parallel operations: the data logger, thermal control system, and the signal electronics. The data logger runs continuously. The thermal control system is the highest power consuming of the three. It is controlled by the data logger as previously described. The signal electronics require a matching positive and negative voltage supply. Therefore,

powered by the main power supply, a high-quality switching power supply is implemented here (10) (11).

2.2 Laboratory Radiometric Calibration

Prior to deployment, GVRs are calibrated in the RSG laboratory using a 1-m spherical integrating source (SIS). During calibration, the GVR and a calibrated radiometer view the exit port of the SIS, which provides the radiance for the two instruments. An absolutely-calibrated ASD spectroradiometer (described in Section 1.2) is currently used as the transfer radiometer source for GVR calibration. The ASD and GVR measure the output radiance from the SIS simultaneously. The calibration coefficient of the i^{th} GVR channel, k_i , is defined as

$$k_i = \frac{L_{e\lambda}}{V_i} \quad (2.1)$$

where $L_{e\lambda}$ [$\text{W}/(\text{m}^2 \cdot \text{sr} \cdot \mu\text{m})$] is the dark-corrected band-averaged hyperspectral radiance measured by the ASD, and V_i [V] is the dark-corrected voltage output of the GVR (10) (11).

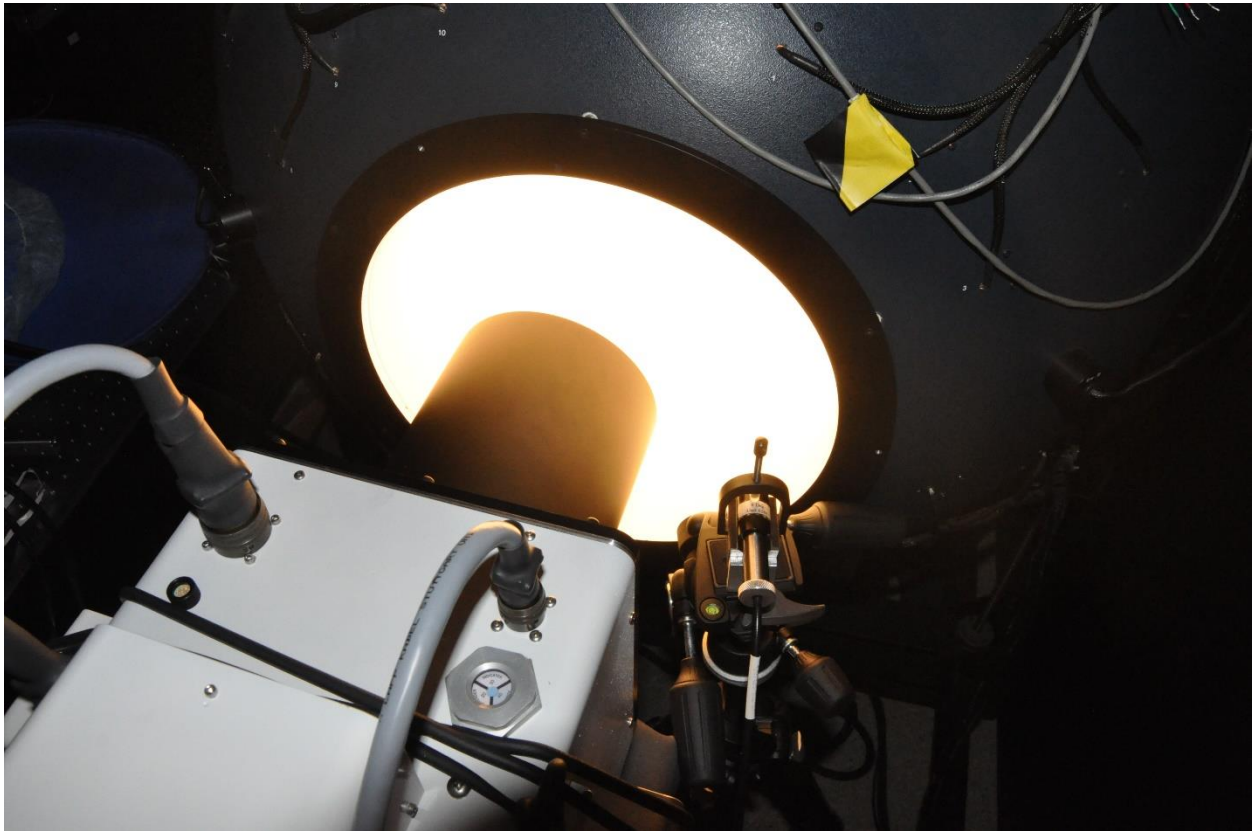


Figure 2.3. GVR head (left) and ASD (right) viewing an SIS during the radiometric calibration of the GVR.

2.3 Application of Spectral Band Adjustment Factors

The relative spectral response (RSR) of radiometric sensors have inherent differences, and are specified based on the phenomenon that is to be observed and detected. This topic has been studied in depth in previous works regarding the sensors on Earth-observing satellites (3) (13). There are many satellites in orbit today that use a wide variety of sensors. The data from these sensors are used to gain a more complete understanding of the Earth's surface and surface processes. Cross-calibration is a well-established technique that is used to compare the radiometric calibration of many differing sensors (14) (15) (16). Cross-calibration uses a well-calibrated sensor as a transfer radiometer, and near simultaneous Earth observation with other sensors to

characterize the sensors. Cross-calibration is used across sensors with significantly varying spectral response. Because of this, the accuracy can suffer because the uncertainties due to RSR differences can be relatively high (17). To combat the disparity, spectral band adjustment factors (SBAF) have been implemented. With prior knowledge of the target, SBAFs can reduce the effects of differing RSRs by considering the spectral profile of a particular target and the RSR each sensor (13) (17).

SBAF correction between multispectral sensors that are calibrated in the laboratory can increase the accuracy of such measurements. The radiometric calibration of the GVRs deployed at RadCaTS are periodically monitored on-site using the cross-calibration technique. Differences in the RSR of the test and reference instruments can increase the uncertainty in the measurements if not taken into account. For example, the RSRs of GVR 24 and the Calibration Test Site SI-Traceable Transfer Radiometer (CaTSSITTR) are shown in Figure 2.4. GVR 24 is currently deployed at RRV and CaTSSITTR is an ultra-portable transfer radiometer that RSG designed for cross-calibration of the GVRs and on-site validation (18). CaTSSITTR is designed with the same band filters as the GVRs, except that it not outfitted with the eighth band (1550 nm) that would be measured by the InGaAs detector (19). Ideally, the two radiometers would have the same spectral response, but in reality, there are differences. The bands with center wavelengths of 400, 450, and 500 nm have very similar RSRs. The bands with the center wavelengths of 550, 650, and 850 nm have relatively moderate difference in RSR, with the 850-nm band showing the smallest difference of the three. The 1000-nm band has a significantly higher difference.

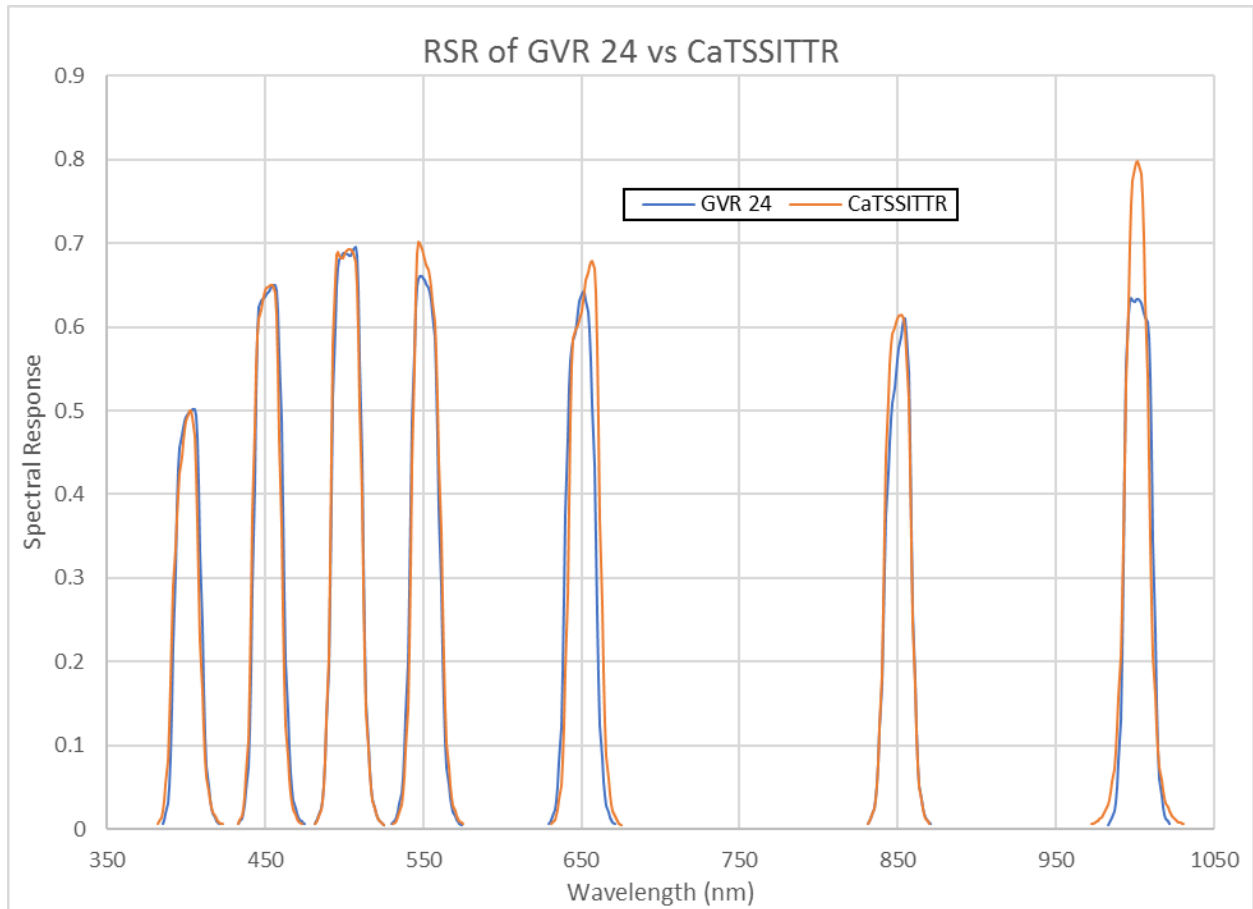


Figure 2.4. Relative spectral response of GVR 24, which is currently deployed in RRV, and CaTSSITTR, which is the transfer radiometer used for cross-calibration. The bands shown have center wavelengths in nm of 400, 450, 500, 550, 650, 850, and 1000.

The equations that define SBAFs for top-of-atmosphere applications (13) shown below have been slightly modified for this work such that

$$\bar{\rho}_{\lambda} = \frac{\int \rho_{\lambda} RSR_{\lambda} d\lambda}{RSR_{\lambda} d\lambda} \quad (2.2)$$

$$SBAF = \frac{\bar{\rho}_{\lambda(A)}}{\bar{\rho}_{\lambda(B)}} = \frac{\frac{\int \rho_{\lambda} RSR_{\lambda(A)} d\lambda}{RSR_{\lambda(A)} d\lambda}}{\frac{\int \rho_{\lambda} RSR_{\lambda(B)} d\lambda}{RSR_{\lambda(B)} d\lambda}} \quad (2.3)$$

$$\bar{\rho}_{\lambda(A)}^* = \frac{\bar{\rho}_{\lambda(A)}}{SBAF} \quad (2.4)$$

where ρ_λ [unitless] is the hyperspectral surface reflectance of RadCaTS, $\bar{\rho}_{\lambda(A)}$ [unitless] is the simulated reflectance for Sensor A, $\bar{\rho}_{\lambda(B)}$ [unitless] is the simulated reflectance for Sensor B, and $\bar{\rho}_{\lambda(A)}^*$ [unitless] is the compensated reflectance for Sensor A using the SBAF to match Sensor B .

To compute the SBAFs and compensated reflectance, a spectral reflectance must be provided as input. The spectral reflectance used in this work was collected using an ASD at RadCaTS on 2 Aug 2017. The 8° ASD foreoptic was positioned in a nadir-viewing configuration 1.87 m above the ground to replicate the spot size of a GVR channel. A two-axis bubble level was used to ensure a nadir view. The sky was clear over RRV, which provided stable illumination conditions during the surface reflectance retrieval. Five data sets were collected, and the surface reflectance was determined using a ratio of the ASD digital numbers from the ground measurements to those obtained over a Spectralon panel. The average reflectance of the five data sets was used as the spectral reflectance, ρ_λ . These data were collected solely as proof of concept of this method, and not for actual cross-calibration. The $RSR_{\lambda(A)}$ and $RSR_{\lambda(B)}$ are relative spectral responses from GVR 24 and CaTSSITTR, respectively (Figure 2.4).

The results from applying SBAFs to GVR 24 for compensation to match CaTSSITTR are summarized in Table 2.1. $\bar{\rho}_{ASD}$ is the average reflectance over the range of each bandwidth [unitless]. $RSR_{GVR\ 24}$ and $RSR_{CaTSSITTR}$ [unitless] are the respective relative spectral responses averaged over each bandwidth and $\bar{\rho}_{GVR\ 24}^*$ [unitless] is the adjusted reflectance measured by GVR 24. Since the SBAF was applied to the $RSR_{GVR\ 24}$, this would also be the adjusted RSR for GVR 24. In practice, the user would apply the SBAF to the reflectance at RadCaTS retrieved by GVR 24. The SBAF improved from the percent difference before applying SBAFs

$\left(\frac{RSR_{GVR\ 24} - RSR_{CaTSSITTR}}{RSR_{CaTSSITTR}}\right)$ to the percent difference after applying SBAFs $\left(\frac{\bar{\rho}_{GVR\ 24}^* - RSR_{CaTSSITTR}}{RSR_{CaTSSITTR}}\right)$ in

all bands except for Bands 2 and 6. This method can be applied to any two radiometers in concordance with the spectral reflectance of the target.

Table 2.1
Effects of applying SBAFs to GVR 24 (deployed at RadCaTS) to match CaTSSITTR via ASD
spectroradiometer reflectance data

Band	ρ_{ASD}	SBAF	$RSR_{GVR\ 24}$	$RSR_{CaTSSITTR}$	$\bar{\rho}_{GVR\ 24}^*$	Difference ratio before SBAF	Difference ratio after SBAF
1	0.2123	1.0166	0.4157	0.3934	0.4089	0.0566	0.0394
2	0.2123	0.9999	0.5677	0.5644	0.5677	0.0059	0.0060
3	0.2485	0.9994	0.6289	0.6345	0.6293	-0.0087	-0.0081
4	0.2997	0.9978	0.5724	0.5857	0.5737	-0.0227	-0.0205
5	0.3418	0.9927	0.5517	0.5868	0.5558	-0.0598	-0.0529
6	0.3764	1.0131	0.4823	0.5135	0.4761	-0.0607	-0.0729
7	0.3723	0.9998	0.5456	0.601	0.5457	-0.0922	-0.0920

Chapter 3: Field Measurements

3.1 Data Acquisition

Currently, there are five stationary GVRs deployed at RadCaTS: four in a nadir-viewing configuration, and one is a viewing configuration similar to the GOES-16 (20). Previous studies have stated that four randomly placed GVRs are necessary to spatially sample the BRDF to within $\pm 2\%$ of the total average of RadCaTS (3). The goal of this work is to find the linear distance that a single GVR has to travel to reduce the standard deviation to within $\pm 2\%$ of the average reflectance of RadCaTS. To achieve this, a measurement approach that was timely, accurate, and repeatable, was created for a field campaign in the summer of 2017. The objective of the field measurements was to translate a portable spectroradiometer in a nadir-viewing configuration across a sample area of the playa at set distances. This was repeated multiple times over multiple days when sky conditions were clear.

An ASD was chosen as the radiometric data collection device due to its mobility, speed of data acquisition, and history of use at RRV. The foreoptic was attached to an aluminum arm to ensure the mounting tripod did not impede the FOV of the ASD. The foreoptic was placed at a height of 1.87 m, which replicates the FOV of a nadir-viewing GVR. The assembly is shown in Figure 3.1.



Figure 3.1. ASD setup at Railroad Valley. The foreoptic is mounted on the aluminum arm on the tripod. The signal electronics are on the table under the laptop and the laptop stored the data taken. Fiber optic runs from the foreoptic to the electronics.

Reflectance data were collected at RadCaTS from 31 Jun – 2 Aug 2017. The process for data retrieval was as follows:

1. Optimize the gain and offset settings of the ASD over the barium sulfate (BaSO_4) panel to ensure it has proper dynamic range and is not saturated.
2. Collect data over the barium sulfate reference panel.
3. Translate the tripod assembly and foreoptic linearly for 91 cm, collecting data over the playa surface every 5 cm. The tripod assembly is moved manually and then leveled using a 2-axis bubble level to ensure the foreoptic is at nadir.

4. Collect data while viewing the same BaSO₄ panel at the end of the measurement cycle.

The BaSO₄ panel measurements before and after the surface measurements are required in order to convert the ASD DNs to reflectance using a simple ratio of ground measurements to panel measurements.

Railroad Valley is located in a high desert climate, and in the summer months the temperature can reach 40°C. During the field campaign in Jul–Aug 2017, there were issues with the ASD overheating during some of the measurements. On 1 Jul, and during round one of 1 Aug, the ASD showed TEC (thermoelectric cooler) errors on the user interface GUI, which meant that the temperature of the electronics was outside of recommended values. The TEC error occurred after the ASD had translated ~75% of the 91 cm for both data collection cycles. Adjustments were made to the measurement protocol in order to reduce overheating. This included shortening data collection times by collecting data every 10 cm, instead of 5 cm, as done in round two of 1 Aug, or by keeping the electronics shaded from the sun, as done on 2 Aug. It is unclear if the high temperature had any effect on the accuracy of the data, however, the first round of data collection on 2 Aug is likely to be the most reliable data as there were no errors, and the sky was clear and relatively stable. As such, the data from this round of retrieval is referred to the most in the following sections. A cloud passed overhead midway through the second round of data collection on 2 Aug, minimizing the usable data. Table 3.1 summarizes the data collection.

Table 3.1. Summary of the conditions and challenges of each reflectance data set collected.

Date	Round	Conditions	Notes
31 Jul 2017	1	Clear	Overheating of electronics
1 Aug 2017	1	Clear	Overheating of electronics
	2	Clear	No overheating problems. Data retrieved every 10 cm.
2 Aug 2017	1	Clear	No overheating problems. Likely best data.
	2	Partly Cloudy	Cloud passed between sun and instruments

3.2 Data Processing

The raw data from the data collection process consists of five files per ASD position (every 5 cm for 91 cm) from 350–2500 nm in 1-nm increments, and the associated digital number. The five measurements are averaged at each wavelength, and become the DN_{ground} input for equation 1.1 from Section 1.2.

$$\rho_{ground} = \rho_{panel} \frac{DN_{ground}}{DN_{panel}} \quad (1.1)$$

Since there were two measurements of the $BaSO_4$ panel (before and after ground measurements) taken for each round, DN_{panel} consists of the average of all ten data sets. With the few exceptions described in Section 3.1, the results are the spectral reflectance of the ground (26.2-cm diameter), ρ_{ground} , every 5 cm, for 91 cm.

3.3 Results

The first round of data retrieved on 2 Aug 2017 is shown as surface reflectance in Figure 3.2. The spectral bands from 1331–1430 nm, 1781–1959 nm, and 2351–2500 nm, have been removed for clarity due to low signal-to-noise (SNR) ratio of the ground data due to atmospheric

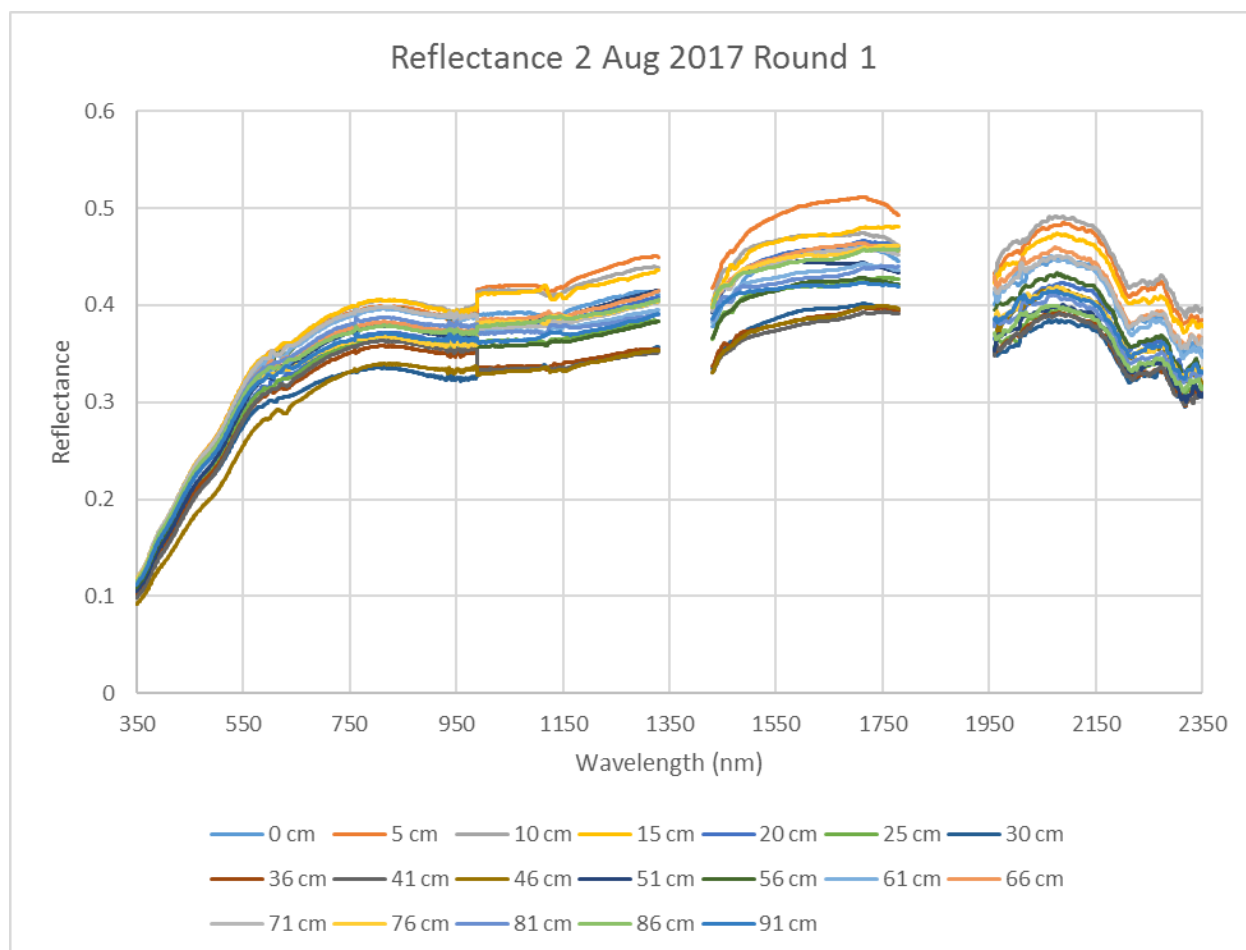


Figure 3.2. Spectral reflectance calculated from data taken by an ASD on 2 Aug 2017. Every 5 cm a new data set is retrieved. At most, there is a difference in reflectance of roughly 0.11.

absorption. Satellite imaging of the Earth in these wavelengths regions is typically avoided, so the reflectance is being ignored in this work. The ASD spectroradiometer has decreased sensitivity in at roughly 2400 nm (21), so the range 2351–2500 nm is ignored. These regions are omitted from the following analysis and results. There is a significant difference in reflectance from one position to another. The second measurement position, at 5 cm, is the most reflective at ~1700 nm, reaching

values above 0.5. However, in longer wavelengths, at the third position of the ASD is the most reflective. The range is ~ 0.12 in reflectance at the largest point.

The average reflectance with the standard deviation is shown in Figure 3.3, which provides an indication of the spatial uniformity of the ground over the translated distance of 91 cm. Recall the ground features of the playa that are plainly visible at ground-radiometer distances (Figure 3.4). These graphs illustrate how they affect the spectral reflectance.

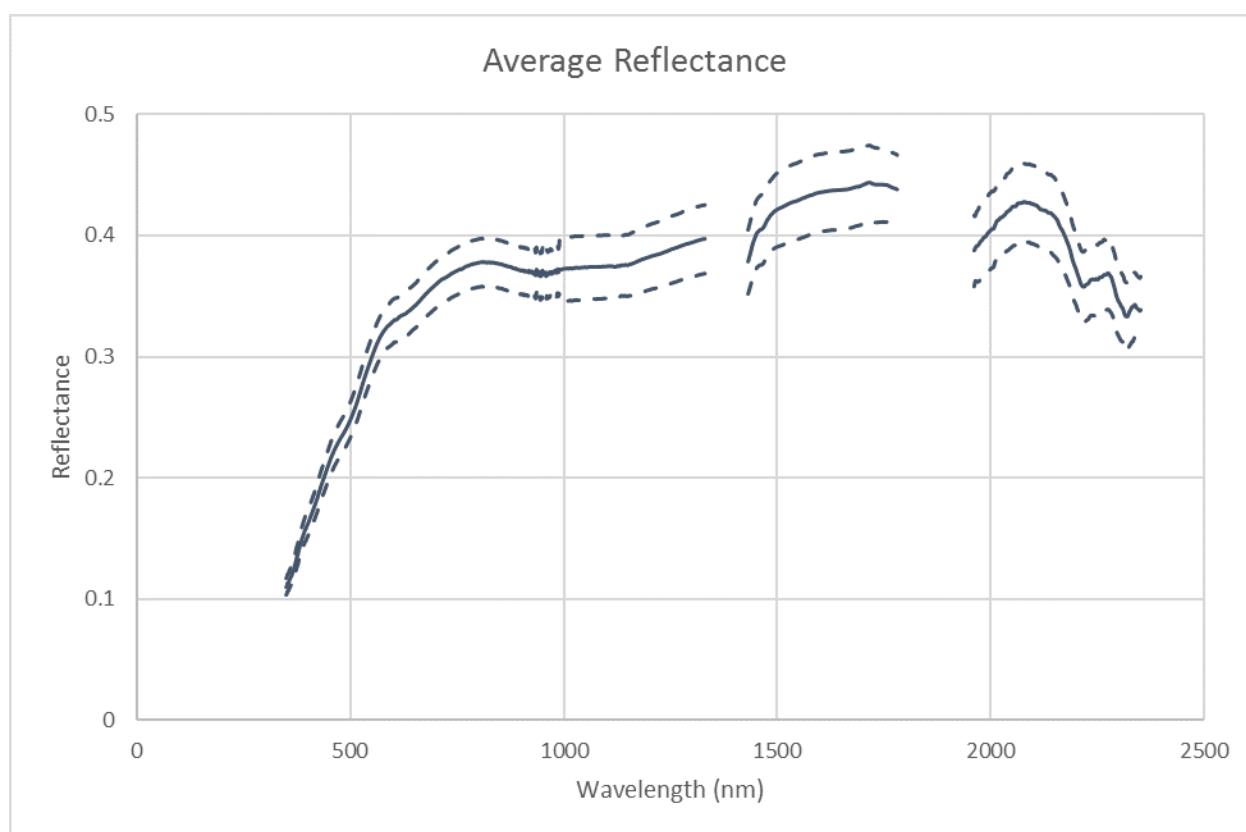


Figure 3.3. Average reflectance on 2 August round 1 as measured by the ASD. The solid line is the average reflectance over 91 cm and the dashed lines are the standard deviation.



Figure 3.4. Top view of the arm, tripod, and foreoptic of the ASD spectroradiometer. The ground has cracks, holes, and bumps that affect the spatial uniformity of the area. Photo taken 31 Jul 2017.

With a goal of minimizing the effects of these small features on the ground-based measurements, care must be given as to how the surface reflectance is analyzed. While the above graphs show how much error can be expected in taking a reflectance measurement, they do not give insight in how to minimize the error. Recall that the GVR has eight channels centered at 400, 450, 500, 550, 650, 850, 1000, and 1550 nm. Figure 3.5 shows the spectral reflectance at each band as the ASD translates across the ground. At 46 cm, there is a distinct drop in reflectance, while at 5 to 15 cm, there is a peak in reflectance. The varying reflectance shows how there can be small areas of low and high reflectance. These peaks and valleys can be minimized using a ground-based system that spatially integrates the reflectance as it translates across the ground.

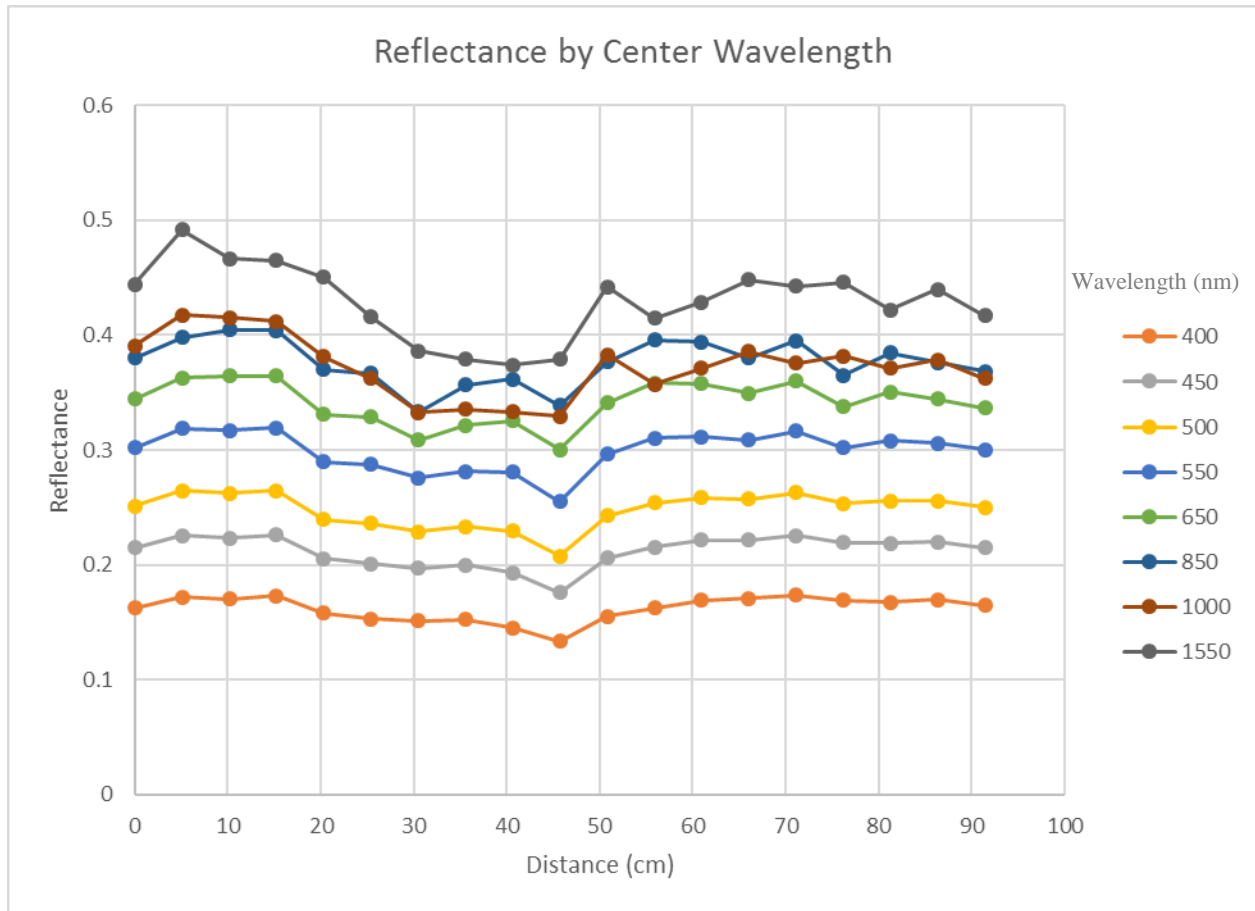


Figure 3.5. Reflectance of RRV by the center bandwidth of each channel on a GVR. Data retrieved using an ASD on 2 Aug 2017 round 1.

Figure 3.6 shows the difference ratio, R , of the cumulative average reflectance data set, \mathbf{P}_{ave} , to the average spectral reflectance as the ASD is translated over the ground such that

$$\mathbf{R} = \frac{\mathbf{P}_{ave} - \overline{\rho_\lambda}}{\overline{\rho_\lambda}} \quad (3.1)$$

$$\mathbf{P}_{ave} = \{\rho_1, \rho_2, \dots, \rho_n\} \quad (3.2)$$

$$\rho_n = \frac{1}{n} \sum_{k=1}^n \rho_{\lambda,k} \quad (3.3)$$

where n is the total number of reflectance data sets retrieved, k is the position of the ASD in terms of data sets, and ρ_λ [unitless] is the spectral reflectance at the given position, k . In the first ten data sets, R varies widely. However, as n increases, more spectral reflectance data are included in P_{ave} ,

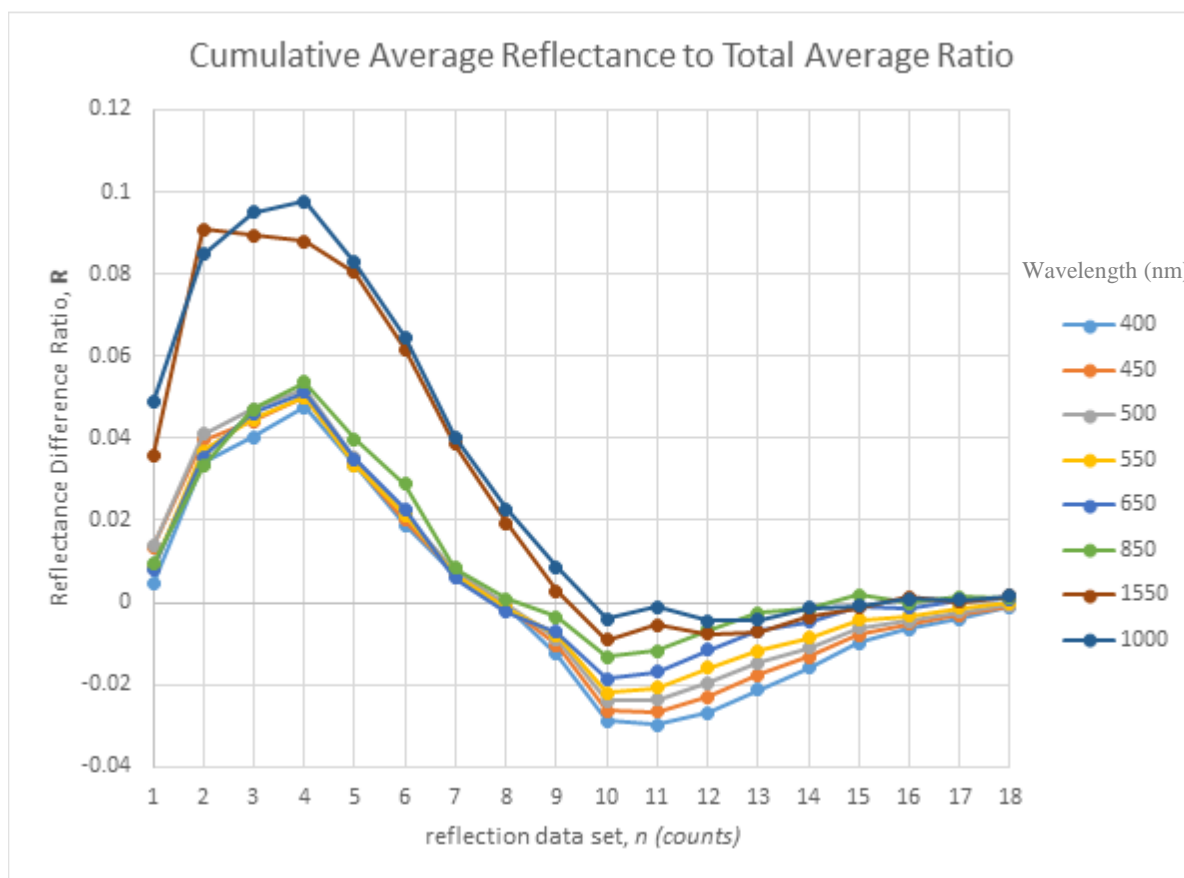


Figure 3.6. Cumulative average reflectance as the ASD translates on the ground. A data set, n , is taken every 5 cm.

making R vary less and, ultimately, approach zero. At reflection data set 14, which is 66 cm from set 1, R is less than ± 0.02 and it stays under for the remainder of the data sets. Where $R \leq 0.02$ for all data collected is shown in Table 3.2. Ratio $R \leq 0.02$ in round 1 of 1 and 2 Aug at 66 cm, $R \leq 0.02$ in round 2 of 1 Aug at 61 cm (data set 7, because spectral reflection was retrieved every 10 cm, not 5 cm), while on the 31 Jun 2017, $R \leq 0.02$ at 81 cm.

Table 3.2. Distance the ASD has translated where $R \leq 0.02$.

Date	Round	Data Set Where $R \leq 0.02$	Distance (cm) Where $R \leq 0.02$
31 Jul 2017	1	17	81
1 Aug 2017	1	14	66
	2	7	61
2 Aug 2017	1	14	66

On 31 Jul, R does not become under 0.02 until the ASD as translated 81 cm and taken 17 data sets, while on the first round of 1 and 2 Aug 2017, it takes until data set 14 at 66 cm. Reflectance is retrieved every 10 cm in round 2 on 1 Aug and $R \leq 0.02$ on data set 7 after the ASD translated 61 cm.

Over the 4 data sets collected, the average distance that the ASD translates across the ground to have the reflective difference ratio be less than or equal to 0.02 is 68 cm. To add room for error, the automated motion control system is designed to translate the GVR optical head 73 cm.

Chapter 4: GVR Translation Stage Design

4.1 System Requirements

The design of the translation stage follows a set of basic system requirements. These requirements were defined from analyzing the data collected from RRV described in Chapter 3, the remoteness of RRV, and the due to the weather conditions that the system is subjected to.

The GVR should travel a minimum of 0.73 m in order to adequately spatially sample the ground. This was determined in Chapter 3 using the surface reflectance analysis of RRV. This requirement should satisfy the goal of measuring the reflectance of RRV to within 2% of the average, using only one GVR.

The focal plane of the GVRs that are currently deployed at RRV are located at a height of 1.5 m above the ground. Therefore, the GVR that is installed on the translation stage will also be mounted at a height of 1.50 ± 0.05 m to account for small variations of the ground. This ensures that the spot diameter of each GVR channel is 26.2 cm, and does not significantly change data processing techniques that are currently in place.

The system is designed so that the shadow of the GVR or the translation stage enters the FOV of the GVR. The current mounting system for static GVRs uses an arm-mount that keeps the GVR a small distance away from the tripod that would otherwise infringe on the FOV (Figure 1.3).

Since RRV is in a remote location, access to electrical power is challenging. A battery and solar panel combination is being used at each GVR, as well as other instrumentation such as the meteorological station, the Cimel solar lunar photometer(s), and also the satellite uplink station. The power system required for the translation mount is similar to the solar charging system used

in the current GVRs. However, it is probable that there will be two solar panels necessary for the GVR and translation stage design: one power the GVR, and one to power the translation stage.

RRV is located in a high desert climate (38.50° latitude, -115.69° longitude). Extreme temperatures, wind, solar radiation, rain, snow, and ice are among the environmental conditions to which equipment are subject. As such, the components involved in the translation stage must be able to withstand being out in the elements. Corrosion and weather resistant materials are to be used wherever necessary to minimize the effects of the environment.

4.2 Translation Stage Design

The general design of the translation stage is shown in Figure 4.1. It consists of a motor-driven ball screw that drives the movement of the GVR, and it is suspended between two posts. Two shafts support the GVR, which are also suspended between the posts. The motor drives the movement of the GVR while it collects radiometric data of the ground.

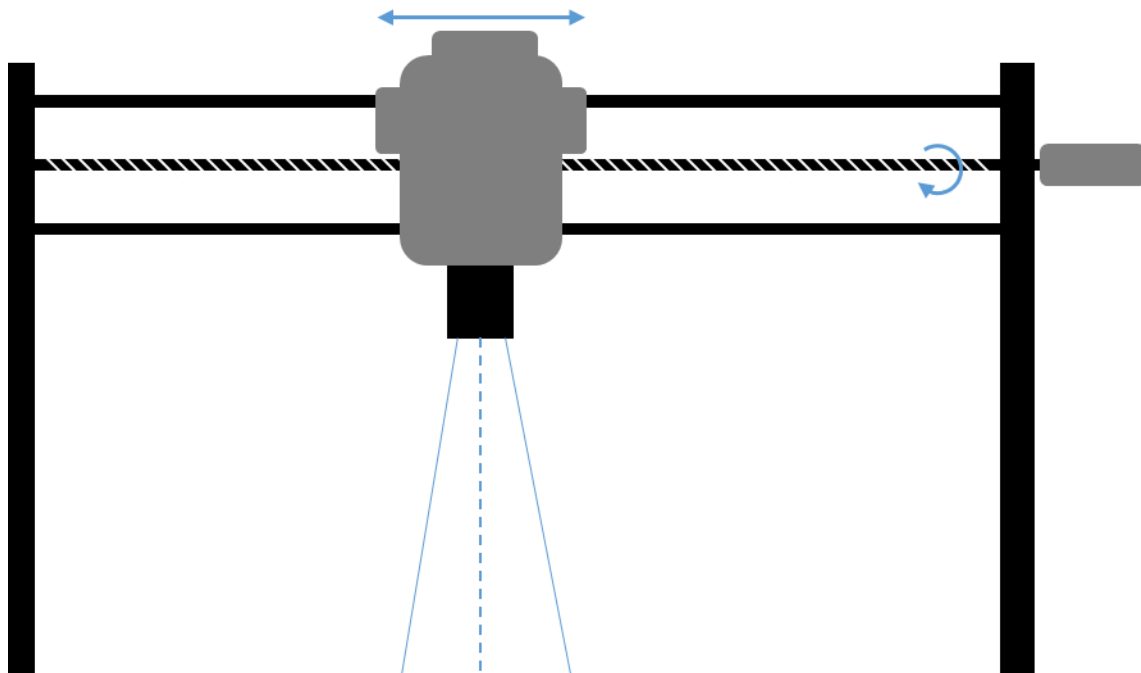


Figure 4.1. Basic design of GVR translation stage. The two support shafts and ball screw are suspended between two posts. A motor drives the ball screw, which drives the linear motion of the GVR.

Heavy-duty steel tripods make up the vertical posts. However, as shown in Figure 4.2, one leg is removed from each tripod, so that the system has four legs when it is fully assembled. The removal of the two legs is required so that the GVR has a clear view of the ground below.

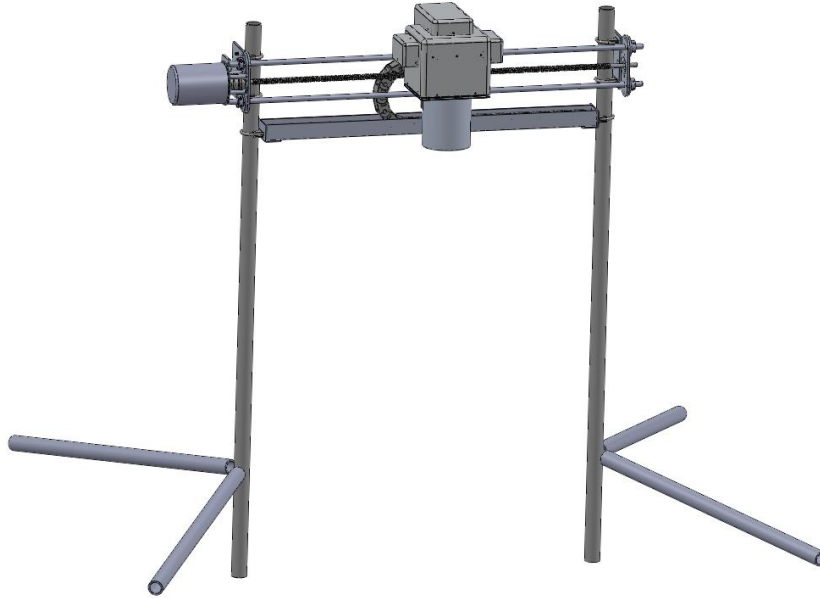


Figure 4.2. SolidWorks model of a GVR mounted on the translation stage. Each tripod has had one leg removed to ensure the GVR has a clear view of the ground. The vertical posts are lower than the legs because they will be inserted into the ground for stability.

The two horizontal support shafts are made from surface hardened 440C stainless steel. This was chosen for its corrosion resistant and stiffness properties. The shafts are 15.875 mm in diameter and have a surface smoothness of 9 μm to minimize friction between themselves and the linear bearings to which the GVR is mounted. The diameter of the shafts was chosen minimize the end slope of the shafts caused by the weight of the GVR. When the GVR is in the middle of the vertical posts as shown in Figure 4.2, the weight of the GVR and the shafts themselves cause the

shafts to bend. The ends of the shafts have a slope that can cause problems when coupled to a motor. The end slope, θ , is estimated such that

$$\theta = \frac{F\ell^2}{16EI} \quad (4.1)$$

$$I = \frac{\pi}{64}d^4 \quad (4.2)$$

where F is the force of the GVR and shafts due to gravity [N], ℓ is the length of the shafts [m], E is the modulus of elasticity [N/m²], which is 205 GPa for 440C stainless steel, I is the second moment of inertia [m⁴] (22). The force F is estimated to be 222 N for the GVR and 19 N for the shaft for a total of 241 N, however, since there are two support shafts, the force on one is half of that, or roughly 121 N. The end slope, θ , is estimated to be 1.09° in reference to an unloaded shaft.

The GVR is mounted on two linear ball-bearings that travel along the shafts (Figure 4.3). The bearings are corrosion resistant, self-aligning up to 1°, and designed for outdoor use. The ball nut consists of ball bearings housed in a stainless steel shell that roll along the raceway of the ball

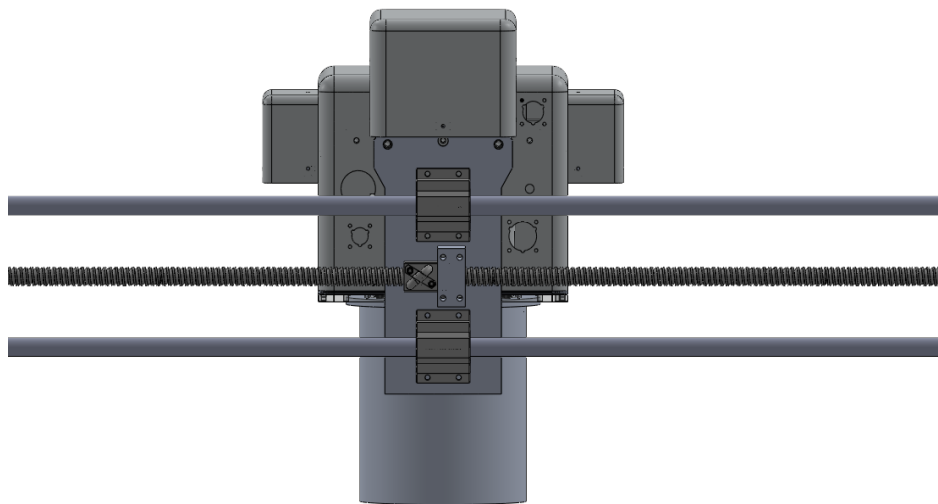


Figure 4.3. Close-up of GVR mounts. The GVR is mounted to two linear bearings that ride on the support shafts. In the center of the shafts is the ball screw, which drives the ball nut that is attached to the GVR as well. Not shown: cables and corresponding protective carriers.

screw. This acts as a precision power screw with little friction. The ball screw is corrosion resistant and suitable for outdoor use as well. The ball screw is made from 17-4 stainless steel, supported at both ends using radial ball bearings, and travels 5.08 mm per turn.

The GVR must be kept in a nadir-viewing configuration for the duration of data retrieval. The GVR is rigidly supported in all axes by two shafts and a ball screw. Thus, the direction that the detectors face is defined by the orientation of the shafts and ball screw. To ensure the GVR view remains as close to nadir as possible, the support shafts and ball screw must be perpendicular to nadir and the plane intersecting the two support shafts must be coincident with nadir. This is accomplished by two sets (one set on each side) of two custom parts shown in Figure 4.4. The T-shaped part supports the shafts and ball screw, while the rectangular mounting plate contains an arc slot that allows the freedom to change the angle at which the T-shaped part is held. Careful positioning of the angle of the T-shaped part, and the height at which the mount plate is attached to the tripod, hold the GVR at the desired location in reference to the ground.

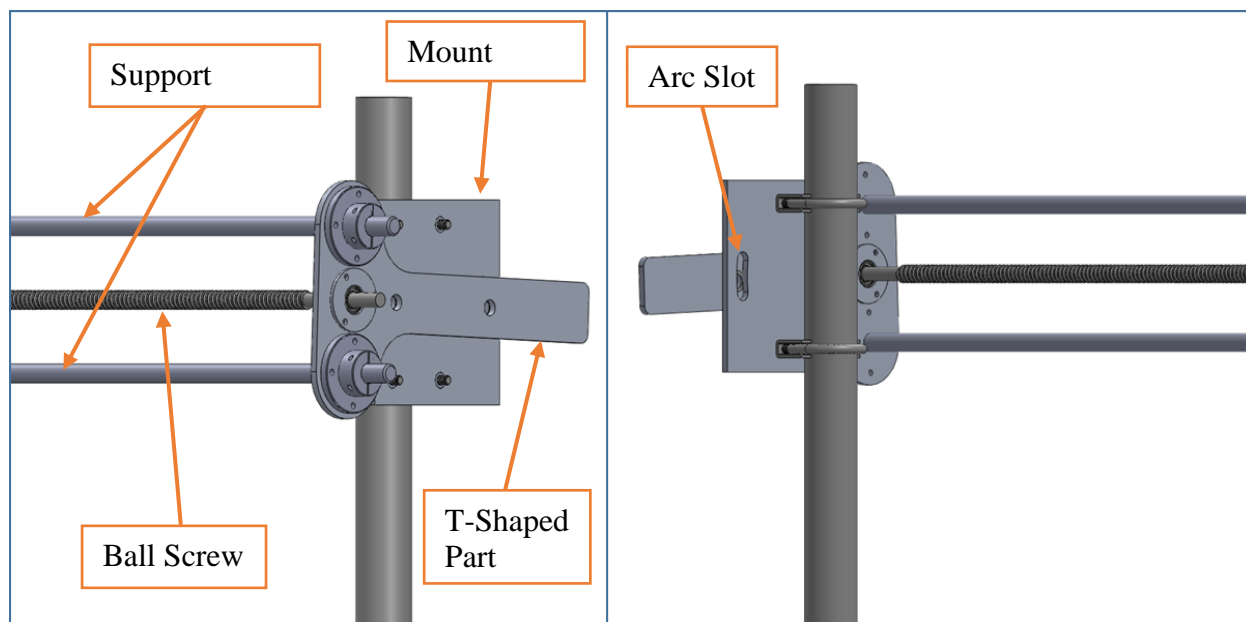


Figure 4.4. Two custom parts define the orientation of the support shafts and ball screw. Left is the view from the exterior of the system and the right is the reverse. The square plate on the right has an arc slot that allows for angle adjustments. Not shown are the necessary fasteners for assembly.

4.3 Motor Considerations

The torque requirement, power source, speed of GVR translation are all important factors when determining the motor. The constant speed torque, T_c [N/m²], consists of the torque due to preload, T_p [N/m²], torque to drive the load, T_d [N/m²], and torque due to friction, T_f [N/m²], such that

$$T_c = T_p + T_d + T_f \quad (4.3)$$

$$T_f = \frac{F_f L}{2\pi\eta} \quad (4.4)$$

where T_* [N/m²] is the torque required, L [m] is the lead of the screw, which is 0.516 mm, and η [unitless] is the efficiency of the ball screw/nut interaction, which typically range 0.7 to 0.9 (23). For this system, minimum friction is desired so no preload is applied to the ball screw ($T_p = 0$).

The dynamic friction force for a linear ball bearing, F_f [N], is

$$F_f = \mu_k W + f_{seal}. \quad (4.5)$$

where the coefficient of dynamic friction, μ_k , for the linear ball bearings is 0.002 to 0.003, W [N] is the weight of the load, and f_{seal} [N] is the seal resistive force, which is typically 2 to 5 N. For the two linear bearings used in the system ($2 \times f_{seal}$), it is expected that F_f is a maximum of 10 N, and therefore, the required torque due to linear ball bearing friction (T_f) is 1.2 mN.

The acceleration torque, T_a , is

$$T_a = T_c + T_{acc} \quad (4.6)$$

$$T_{acc} = J\omega' \quad (4.7)$$

$$\omega' = \frac{2\pi N}{60t} \quad (4.8)$$

where T_a [N/m²] is the total torque during acceleration, T_{acc} [N/m²] is the torque due to acceleration, J [kg m²] is the inertia of the system, ω' [rad/s²] is the angular acceleration, N [rpm] is the angular velocity, and t [s] is acceleration time. The acceleration time varies based on how the motor is controlled. Table 4.1 shows the total torque during acceleration changing with varying time of acceleration. The rotational speed of 65 rpm was chosen because it is the load speed of the motor. However, it can also vary. The rotational speed defines how fast the GVR is translated

Table 4.1. Estimates of torque required due to acceleration for a changing time of acceleration.

J (kg m ²)	N (rpm)	t (s)	ω' (rad/s)	T_a (mN m)
8.64E-05	65	1	10.472	2.70
8.64E-05	65	0.5	20.944	3.29
8.64E-05	65	0.25	41.888	4.47
8.64E-05	65	0.125	83.776	6.82
8.64E-05	65	0.0625	167.55	11.52

along the linear path. Defining a good speed is subjective, but it should be at a level that is reasonable for a ~23-kg high-quality spectroradiometer to travel. 65 rpms converts to 8.6 mm/s. Unsurprisingly, the torque requirement increases as the time of acceleration decreases. The challenge is to use a motor that has a suitable torque output, rpm output, and be powered by 12 or 24 V_{DC}. The Hansen 121-82416-27C motor is an appropriate choice. It consists of a 24-V gear motor, planetary gearbox, and a 100-count/revolution encoder. The output is 65 rpm, which translates to a linear speed of 5.6 mm/s. This motor supplies a torque of 2.37 N m, which is much greater than the requirement shown in Table 4.1. However, it is prudent to use a motor that is overpowered because of the remoteness of RRV, and the possibility of dust accumulation on the support shafts and ball screw.

A disk-type coupler is used to couple the motor to the ball screw. It is a flexible shaft coupler that allows for an angular misalignment of 2° and an axial misalignment of 0.71 mm, both

of which are acceptable in order to remain within the expected uncertainties. The misalignment analysis is summarized in Appendix B.

4.4 Translation Stage Electronics

The motor is controlled by a basic central processing unit (CPU) in conjunction with a DC motor output stage, which also powers and receives input from the encoder. For testing purposes, the CPU communicates with a laptop via Ethernet in order to drive the motor. When deployed, the data logger provides the trigger, and the CPU will execute its pre-programmed routine. The CPU and DC motor output stage have operating temperature ranges of -25°C to 85°C , and 0°C to 55°C , respectively. Safeguards will be put in place through software control to prevent the operation of the translation stage when the ambient temperature is below 0°C . The CPU and DC motor output stage are to be powered by a 24-V battery and solar panel system that is separate from the one that powers the GVR. The design has yet to be finalized but, is likely to be similar to that of the GVR power system.

Various power and data cables run from the GVR to the data logger and power system. These are housed in a snap-together cable carrier that provides protection and support. The cable carrier is supported by a trough as shown in Figure 4.5.

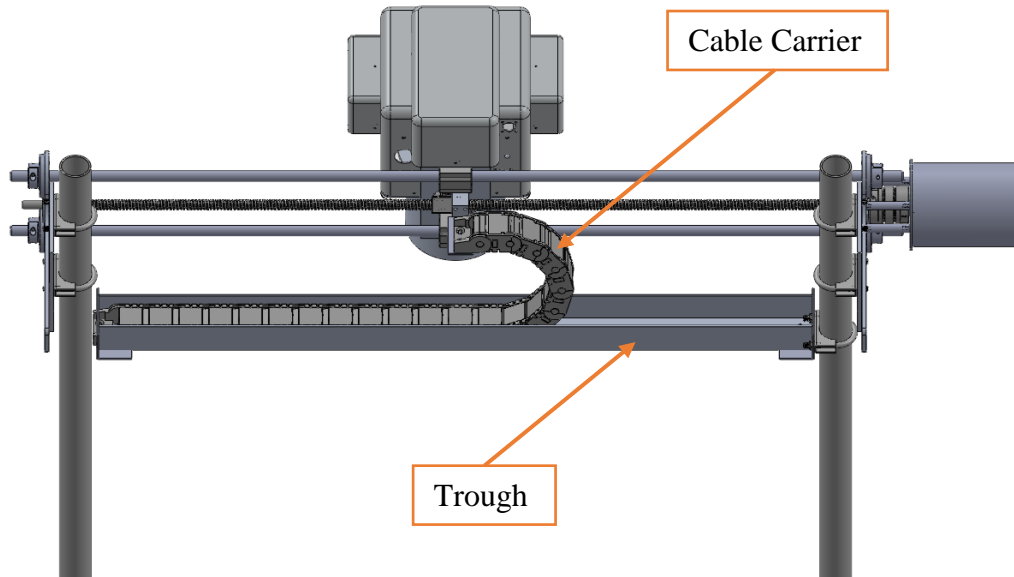


Figure 4.5. Cable carrier providing protection and support for the GVR cables. The carrier is supported by a trough. Not shown are the various cables from the GVR.

Chapter 5: Conclusion and Future Work

5.1 Conclusion

This thesis presents a design to improve the spatial sampling of the automated ground-based radiometric calibration system that the Remote Sensing Group of the University of Arizona operates at RRV. The linear translation of a GVR head by a ~ 73 cm is expected to decrease the standard deviation to within $\pm 2\%$ of the average reflectance of RadCaTS. The motion-controlled linear translation system described in this work is shown to be a viable solution. The materials and electronics used are suitable for use in harsh environments with minimal maintenance and the entire system is expected to cost roughly \$5,000 USD.

5.2 Future Work

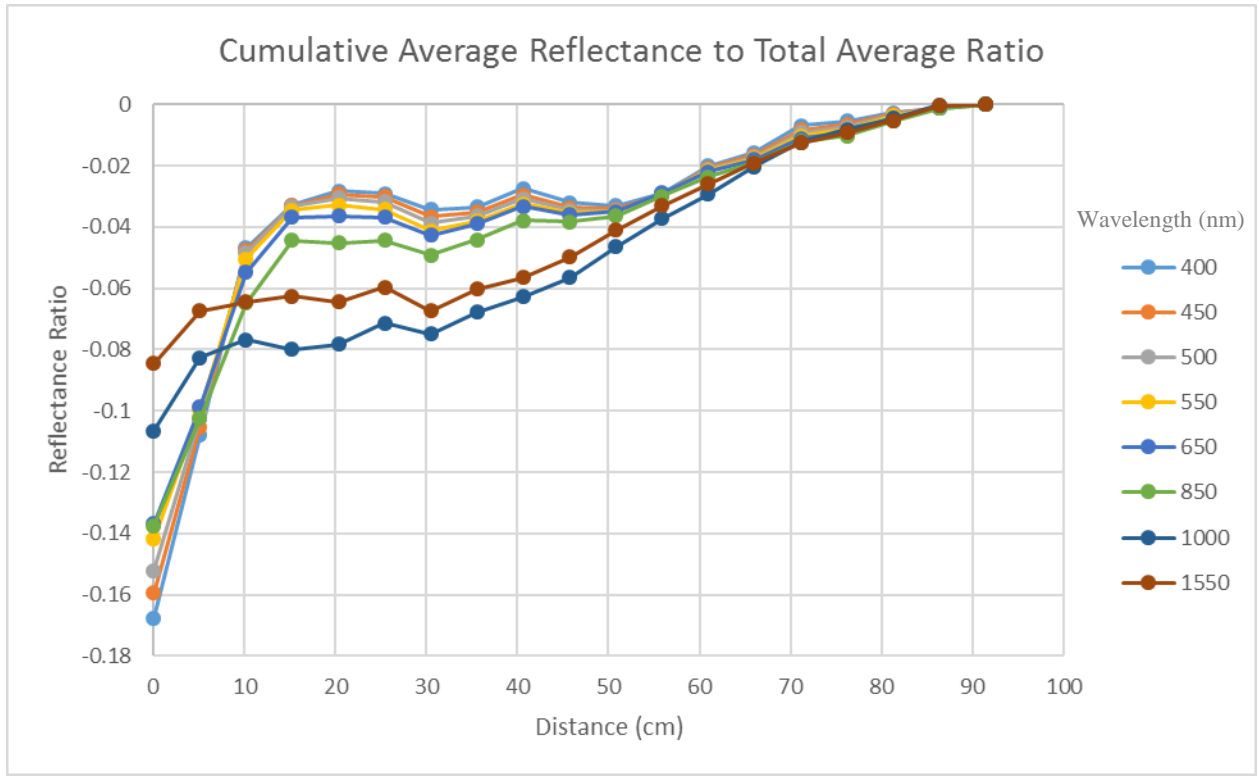
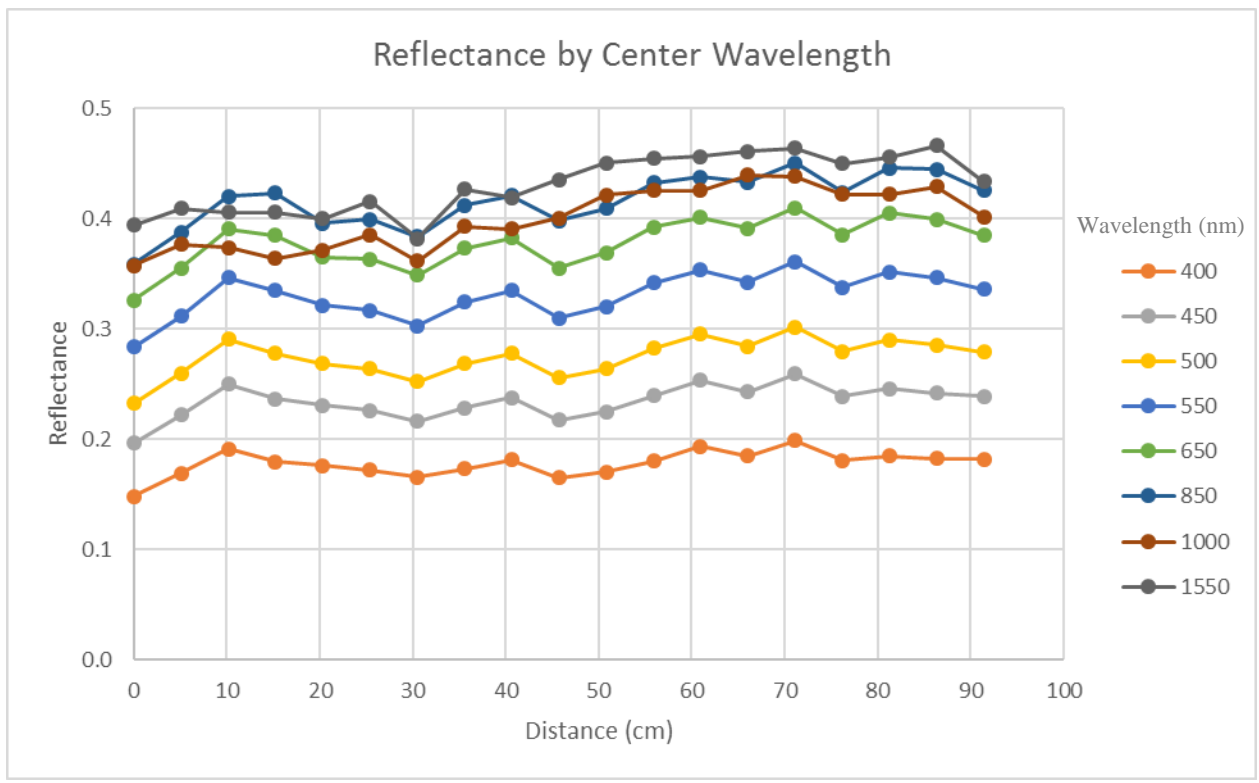
The motion-control system is a prototype that could be updated and/or improved for future versions. The motion and data collection algorithm can be modified and improved upon once the system is deployed at RadCaTS. The data that were collected in 2017 to support the mechanical design requirements of the GVR translation stage were spatially sampled every 5 cm. However, it may be advantageous to collect data at smaller intervals using the fully-autonomous system described in this work. There are plans to analyze multiple sets of data that are collected at varying spatial sampling at the College of Optical Sciences at the University of Arizona. RRV soil has been transported to the college for use in a box that fills the entirety of the FOV of the GVR for the full translation length. The box containing the soil can be flooded with water and let dry to mimic the conditions at RRV.

It is expected that there will be a need for increasing precision in calibration techniques for remote sensors as time moves forward. The motion-control system described here can be

applied to all of the GVRs to improve the spatial sampling of the RadCaTS site at RRV. The improved spatial sampling will reduce the surface reflectance uncertainty, and therefore reduce the uncertainty in the overall RadCaTS methodology.

**Appendix A: Reflectance Analysis from Field Campaign Jul–Aug
2017**

A.2 1 Aug 2017: Collection 1



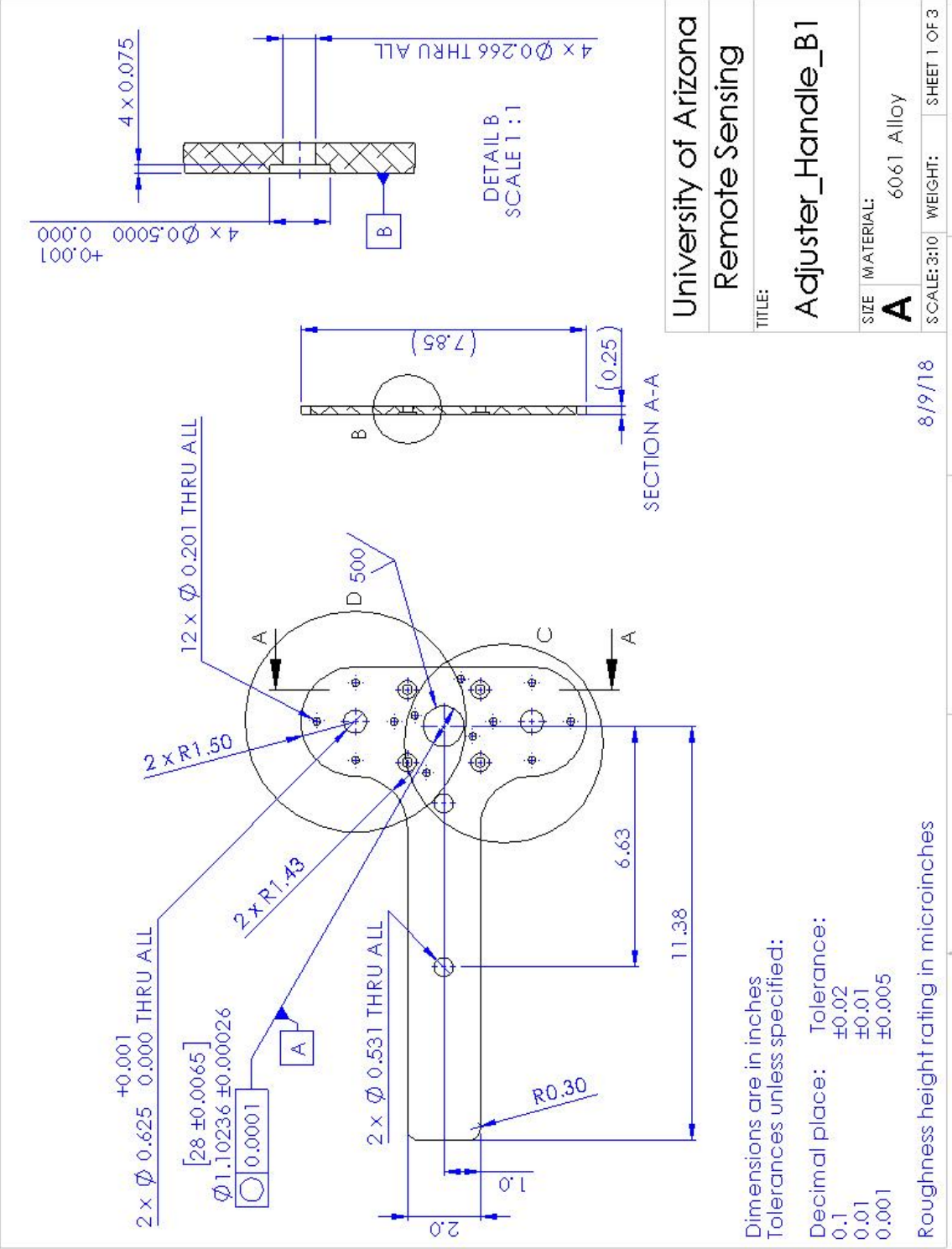
Appendix B: Ball Screw to Motor Shaft Parallel Error

Part	Feature	Instances	Tolerance (mm)	Type
Hansen motor	Cylindrical Locator	1	0.05	Concentricity
Custom Motor Mount	Standoff Locators	4	0.0254	Position
Custom Adjustor	Standoff Locators	4	0.0254	Position
SKF Ball Bearing	Radial Runout	1	0.01	Runout
Total Parallel Error RSS (mm)	0.09			

The tolerance for the motor is an estimation based on typical tolerances of similar DC motor locators. The tolerance for the customs parts are specified in the engineering drawings and the ball bearing radial runout is provided by the manufacturer, SKF.

Appendix C: Custom Parts

C.1 Adjustor Handle 1



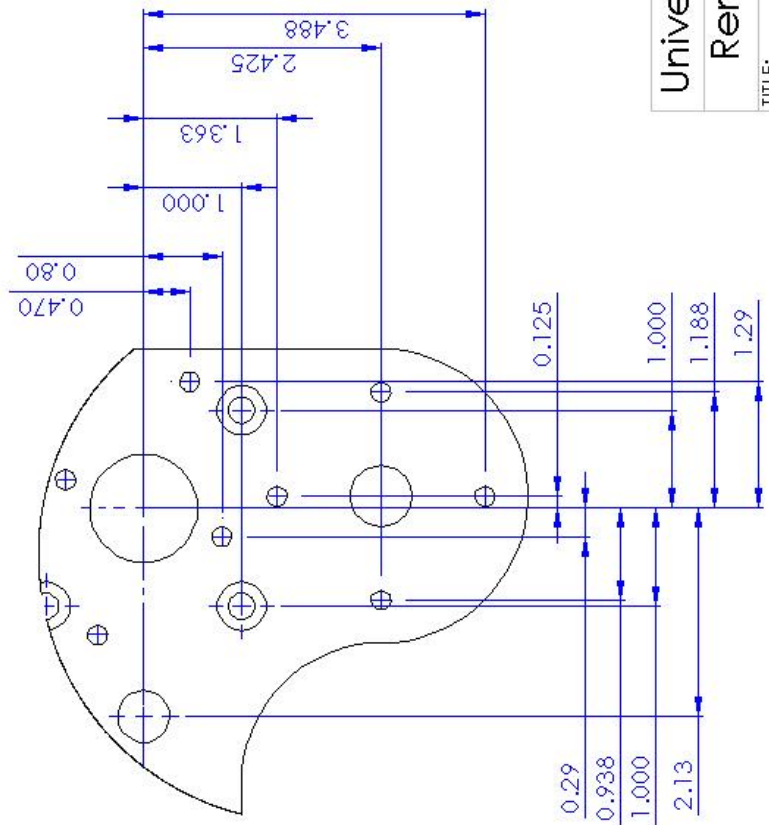
Dimensions are in inches
 Tolerances unless specified:
 Decimal place: Tolerance:
 0.1 ±0.02
 0.01 ±0.01
 0.001 ±0.0005

Roughness height rating in microinches

University of Arizona	
Remote Sensing	
TITLE: Adjustor_Handle_B1	
SIZE	MATERIAL:
A	6061 Alloy
SCALE: 3:10	WEIGHT:
SHEET 1 OF 3	

8/9/18

1 2 3 4 5



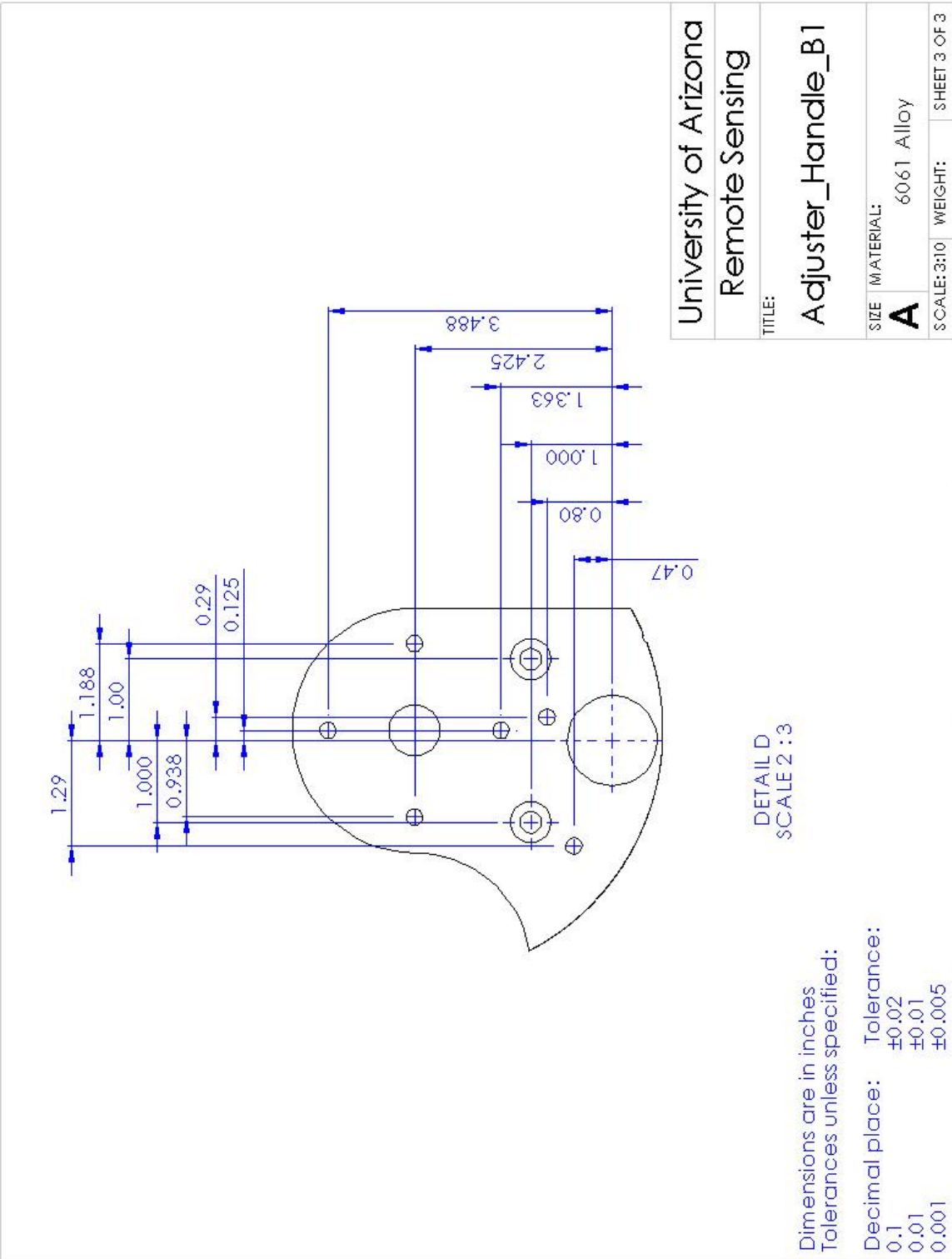
DETAIL C
SCALE 2 : 3

Dimensions are in inches
Tolerances unless specified:

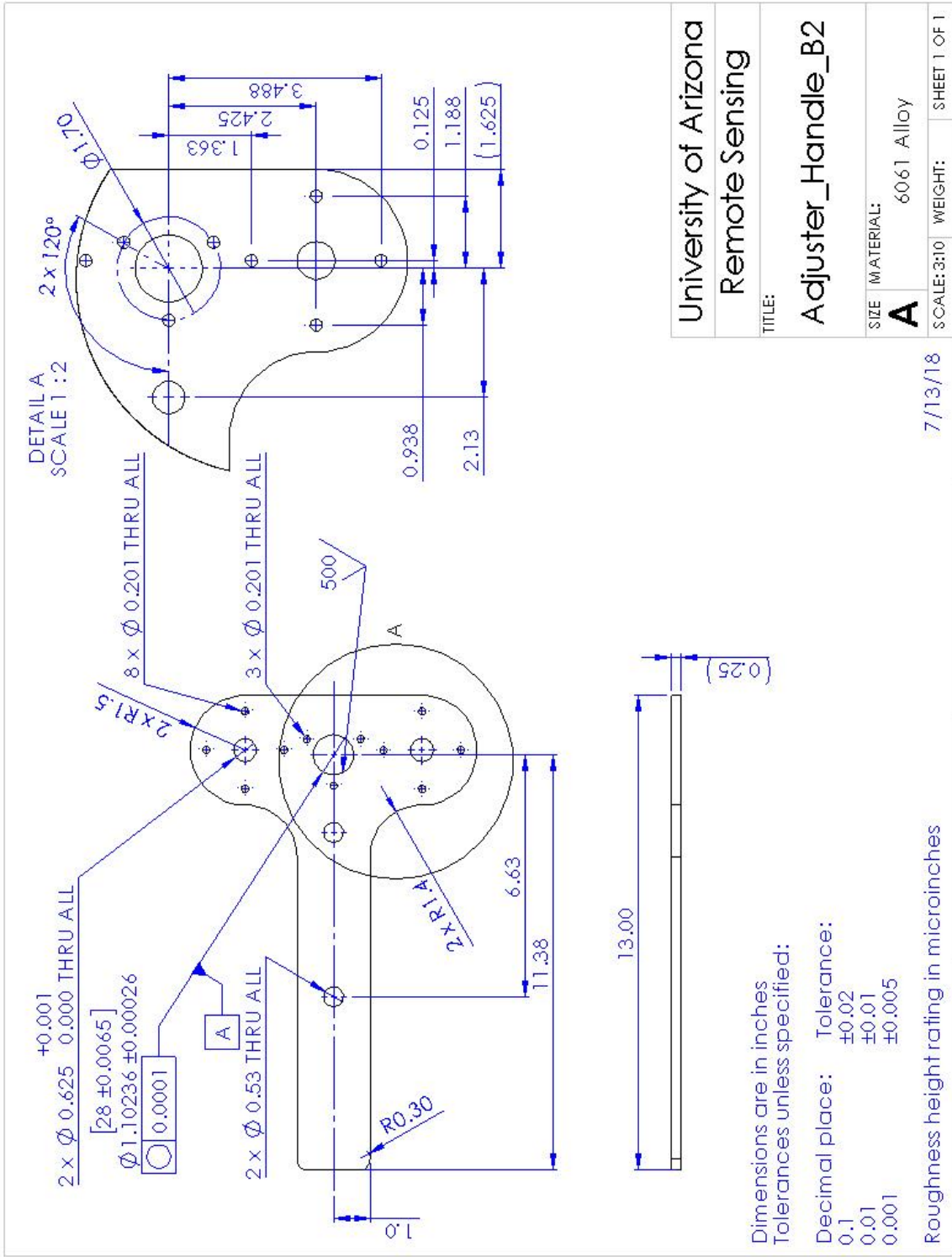
Decimal place:	Tolerance:
0.1	±0.02
0.01	±0.01
0.001	±0.005

University of Arizona Remote Sensing	
TITLE: Adjuster_Handle_B1	
SIZE	MATERIAL:
A	6061 Alloy
SCALE: 3:10	WEIGHT:
	SHEET 2 OF 3

1 2 3 4 5

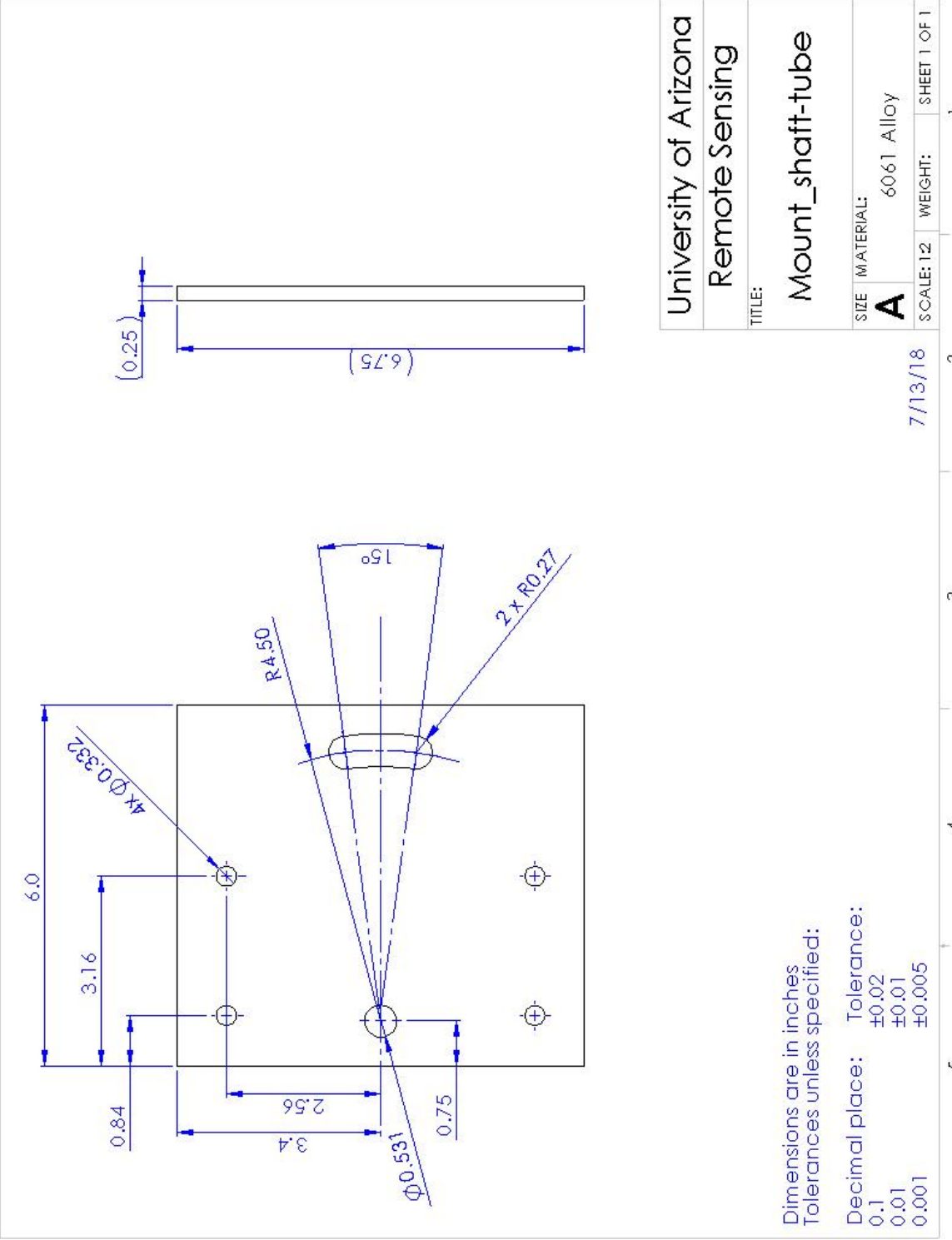


C.2 Adjustor Handle 2

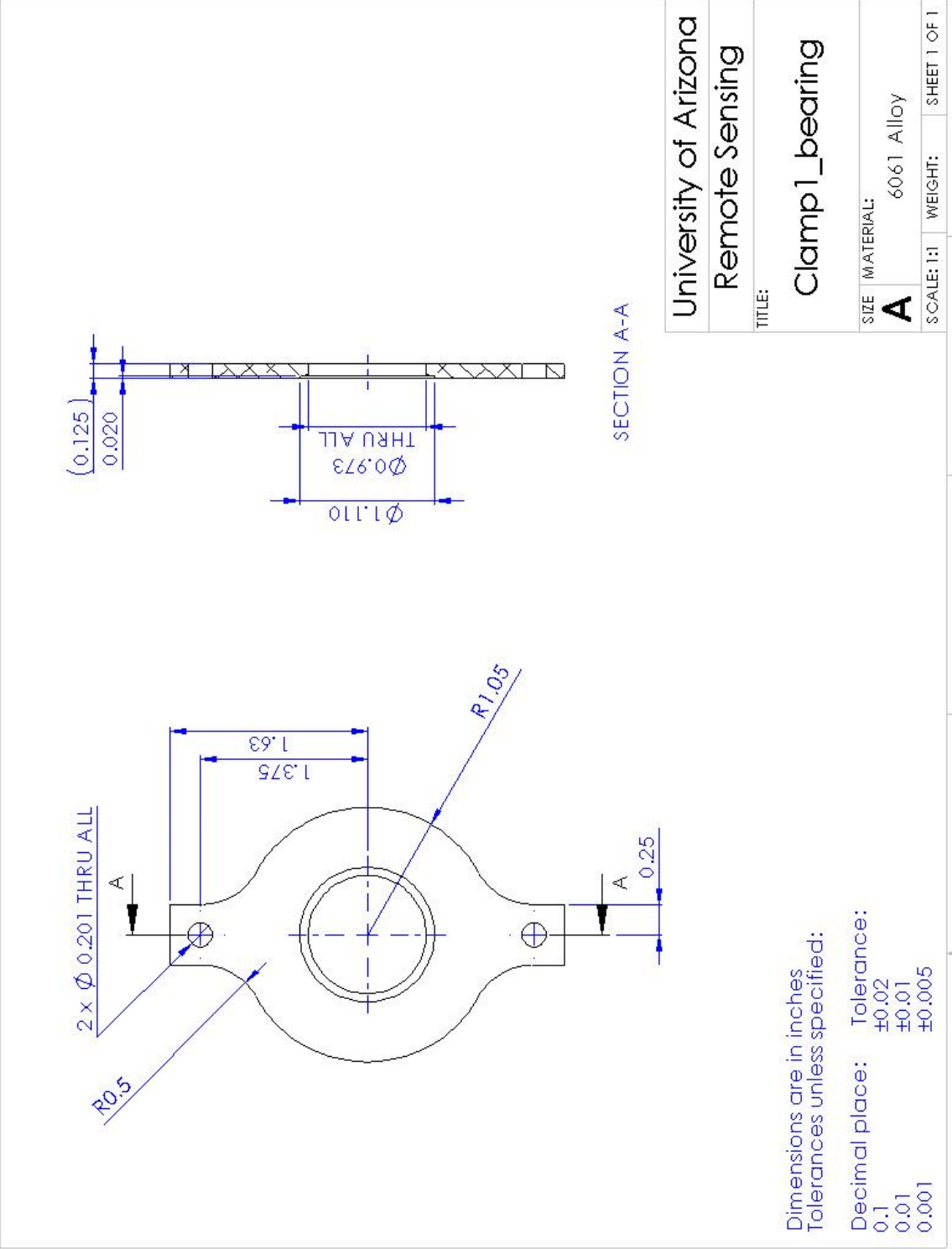


University of Arizona
Remote Sensing
TITLE:
Adjustor_Handle_B2
SIZE:
MATERIAL: 6061 Alloy
A
SCALE: 3:10
WEIGHT:
SHEET 1 OF 1

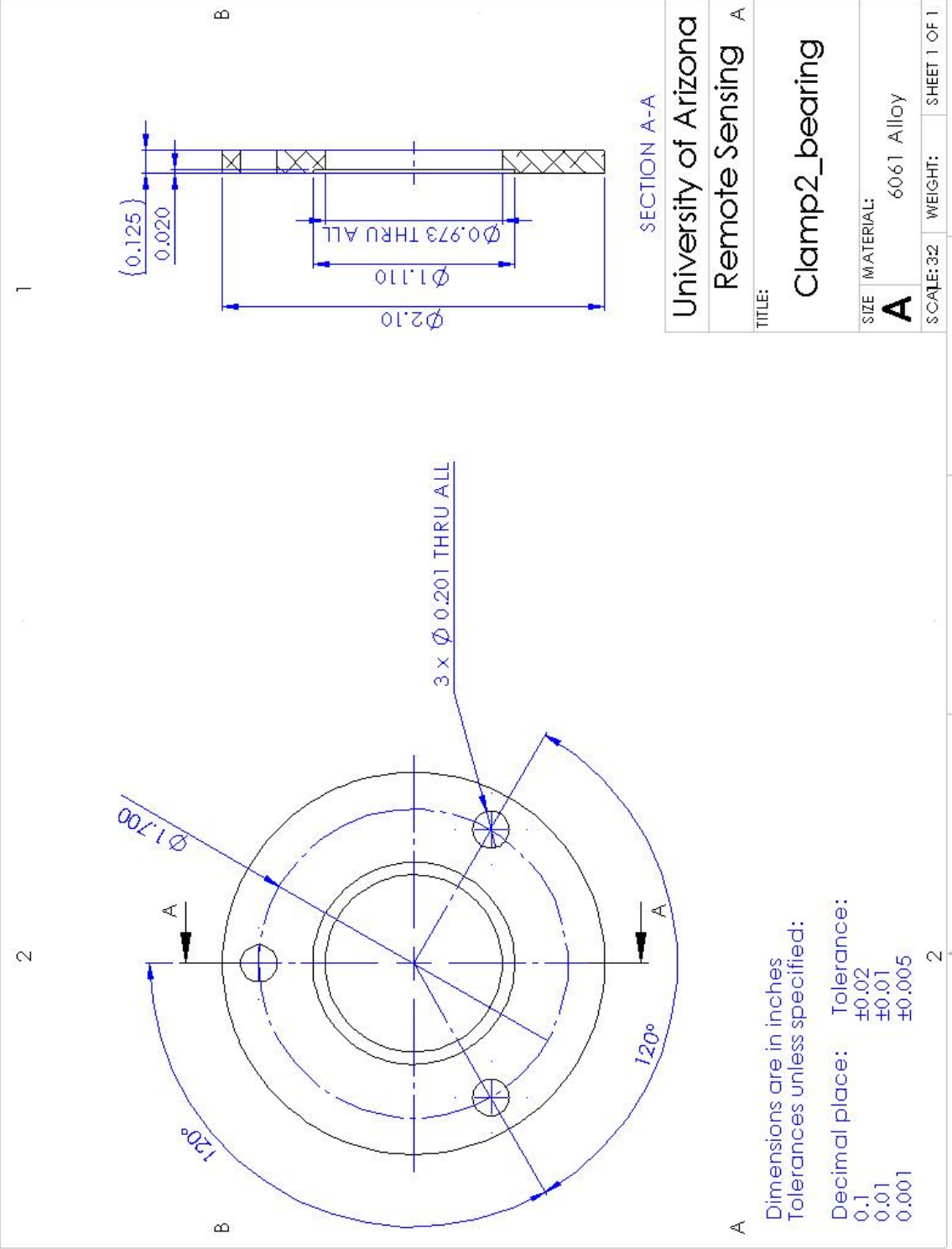
C.3 Tripod Shaft to Adjuster Handle Mount



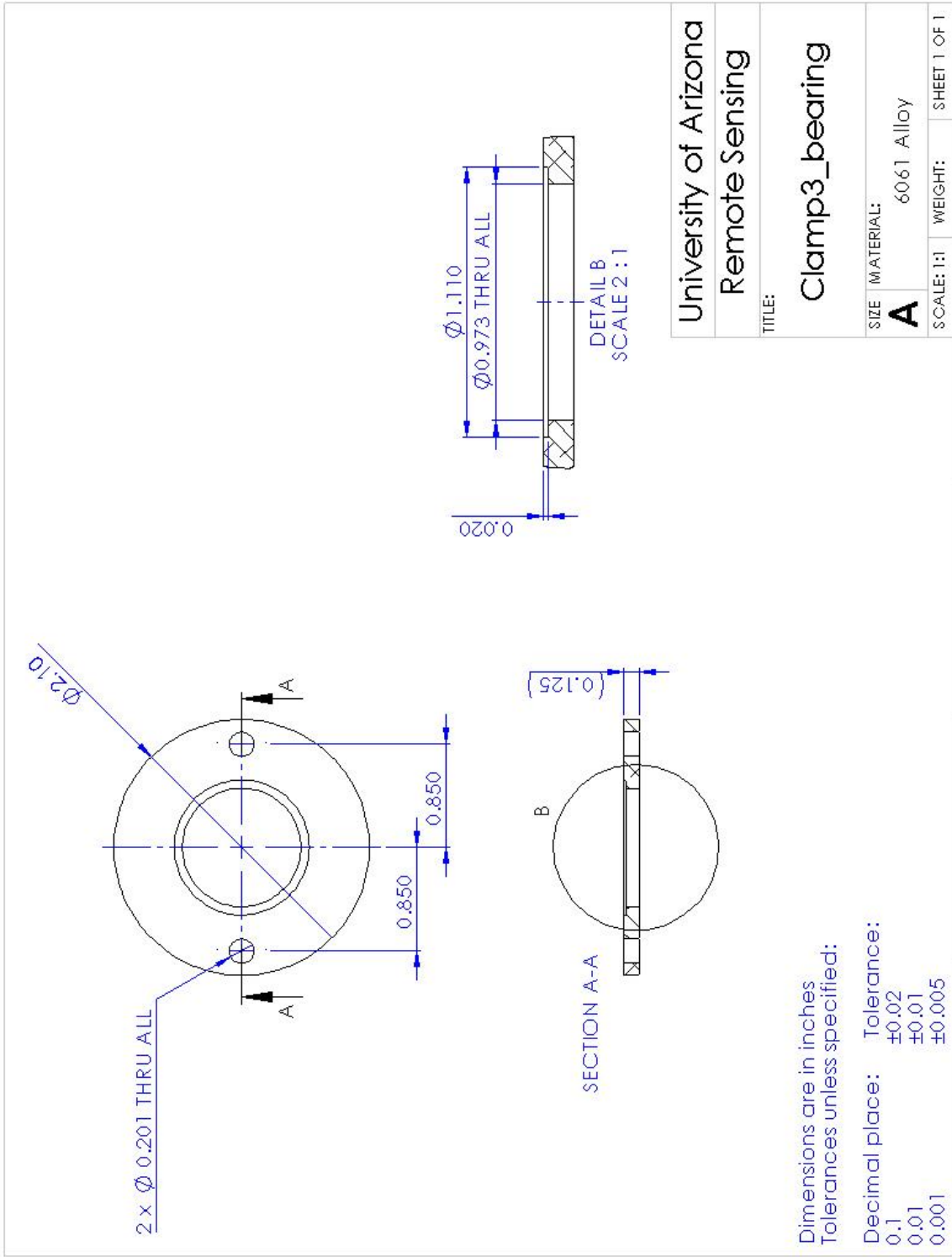
C.4 Clamp 1 for Bearing. Qty. 2



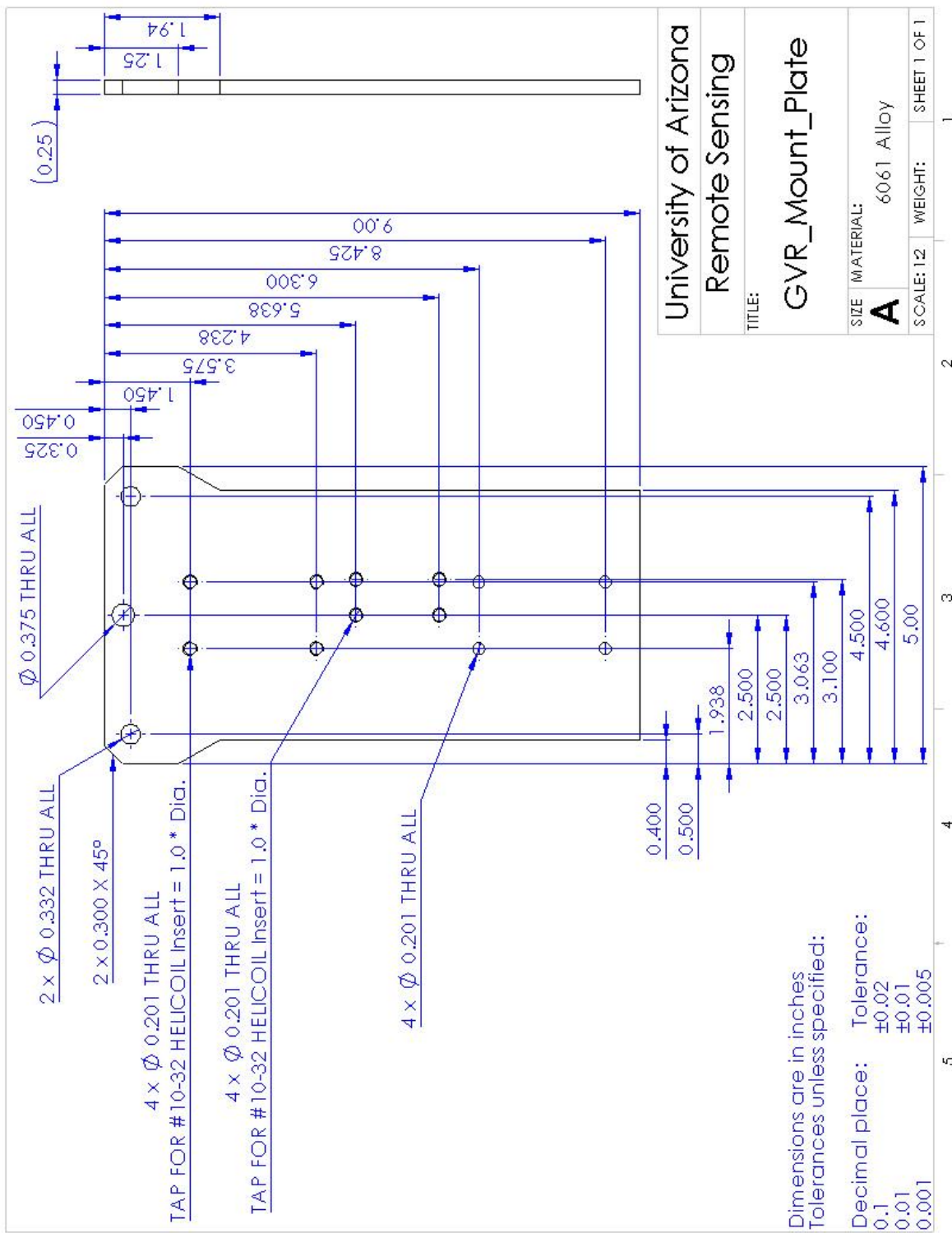
C.5 Clamp 2 for Bearing



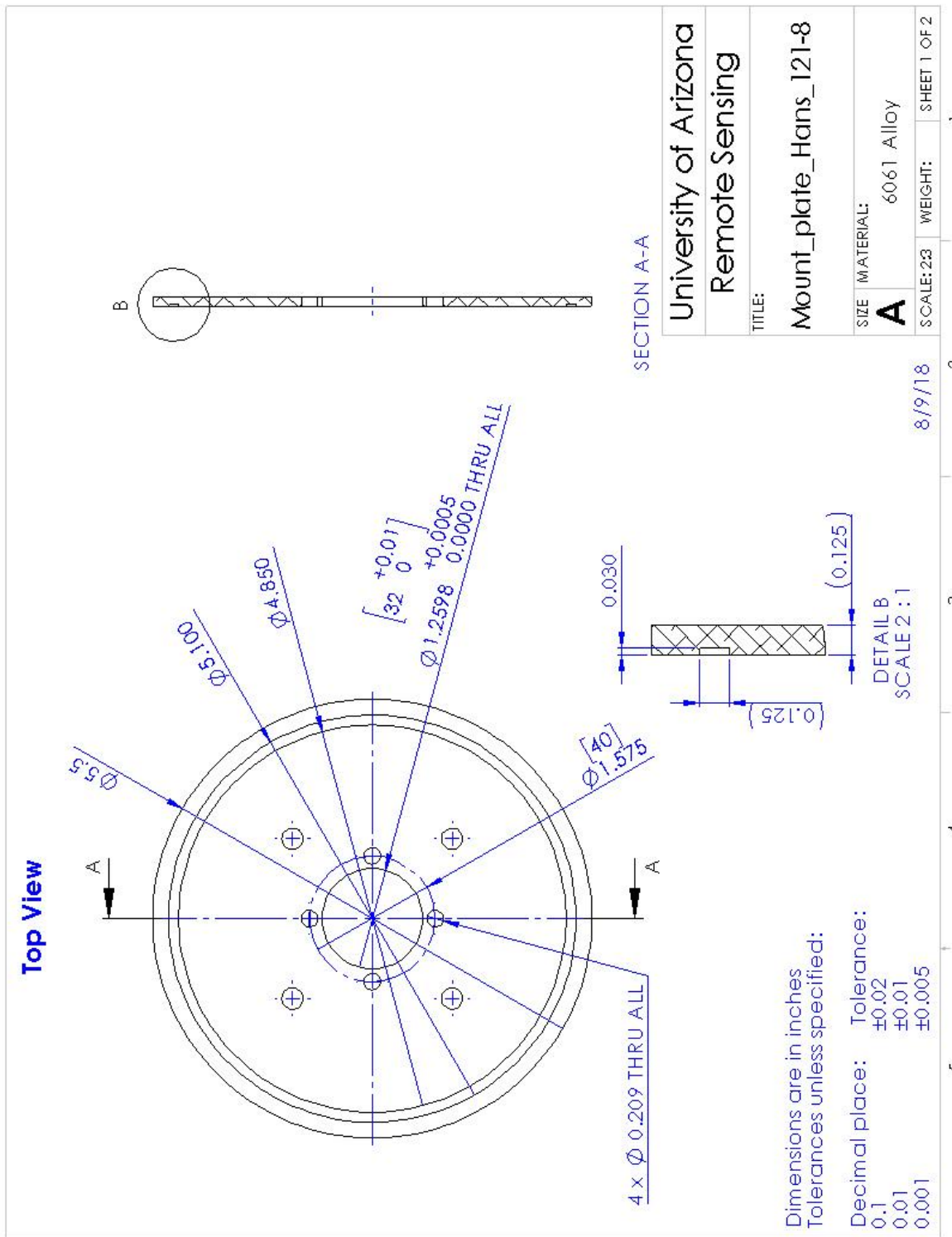
C.6 Clamp 3 for Bearing

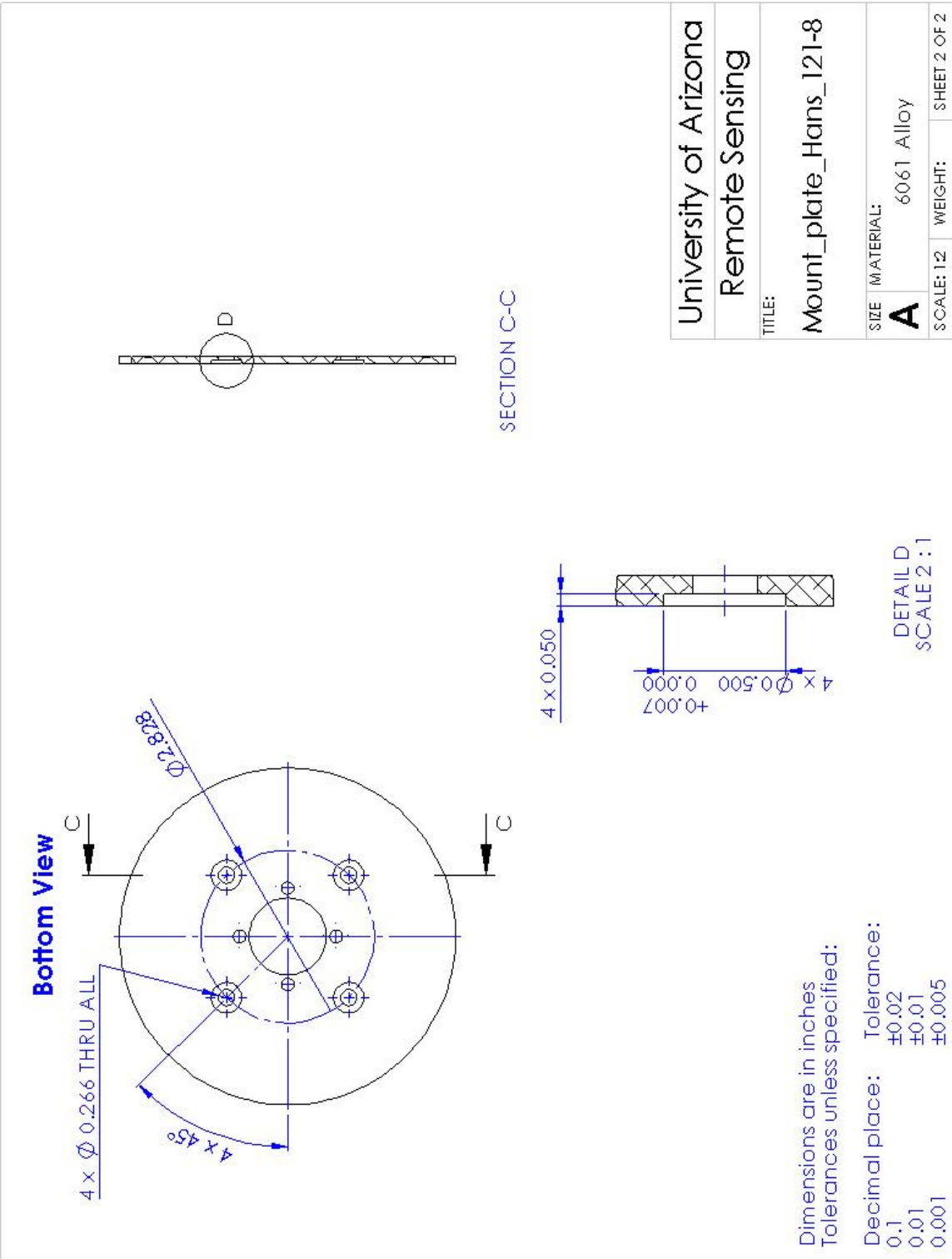


C.7 GVR Mount Plate

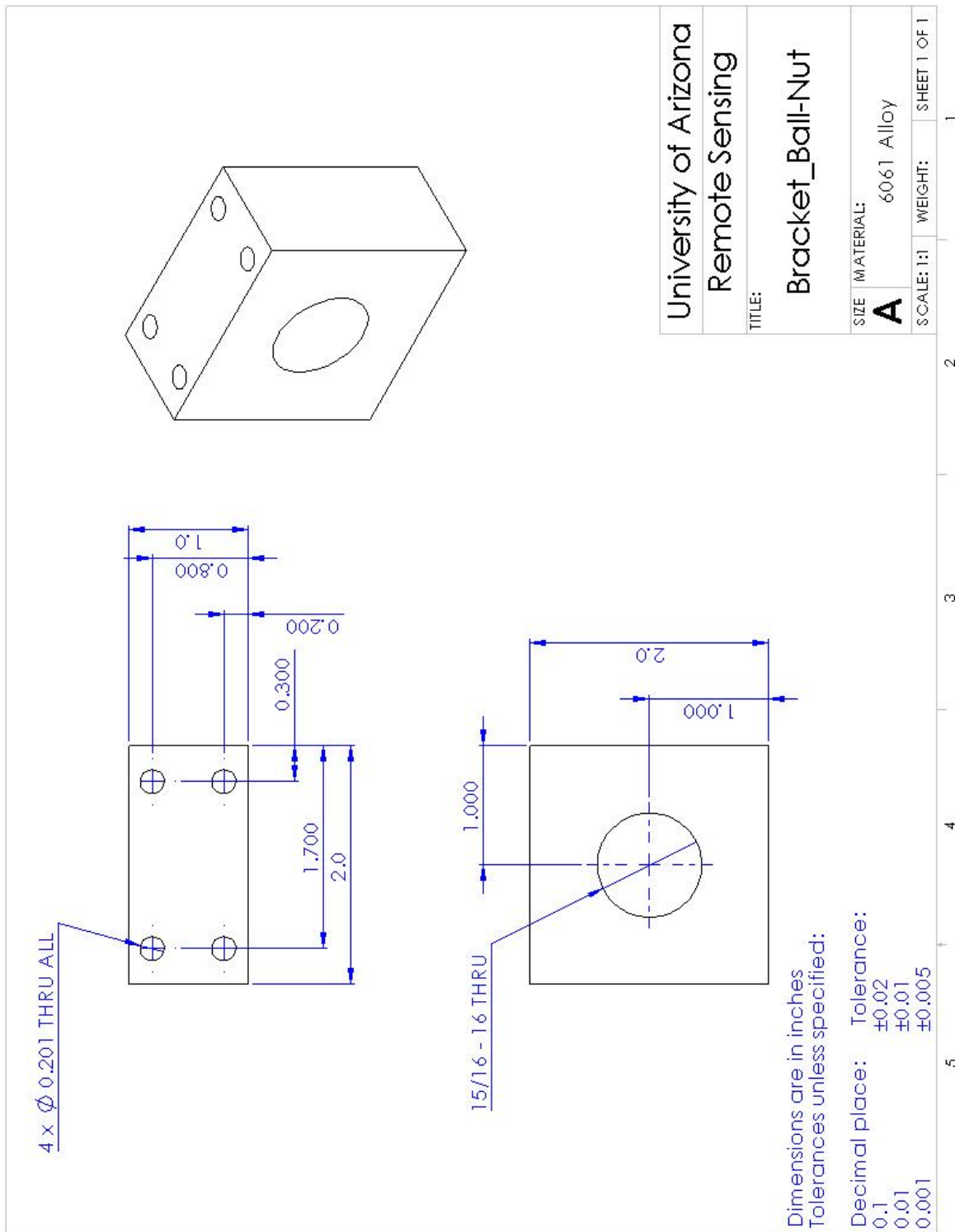


C.8 Motor Mount Plate

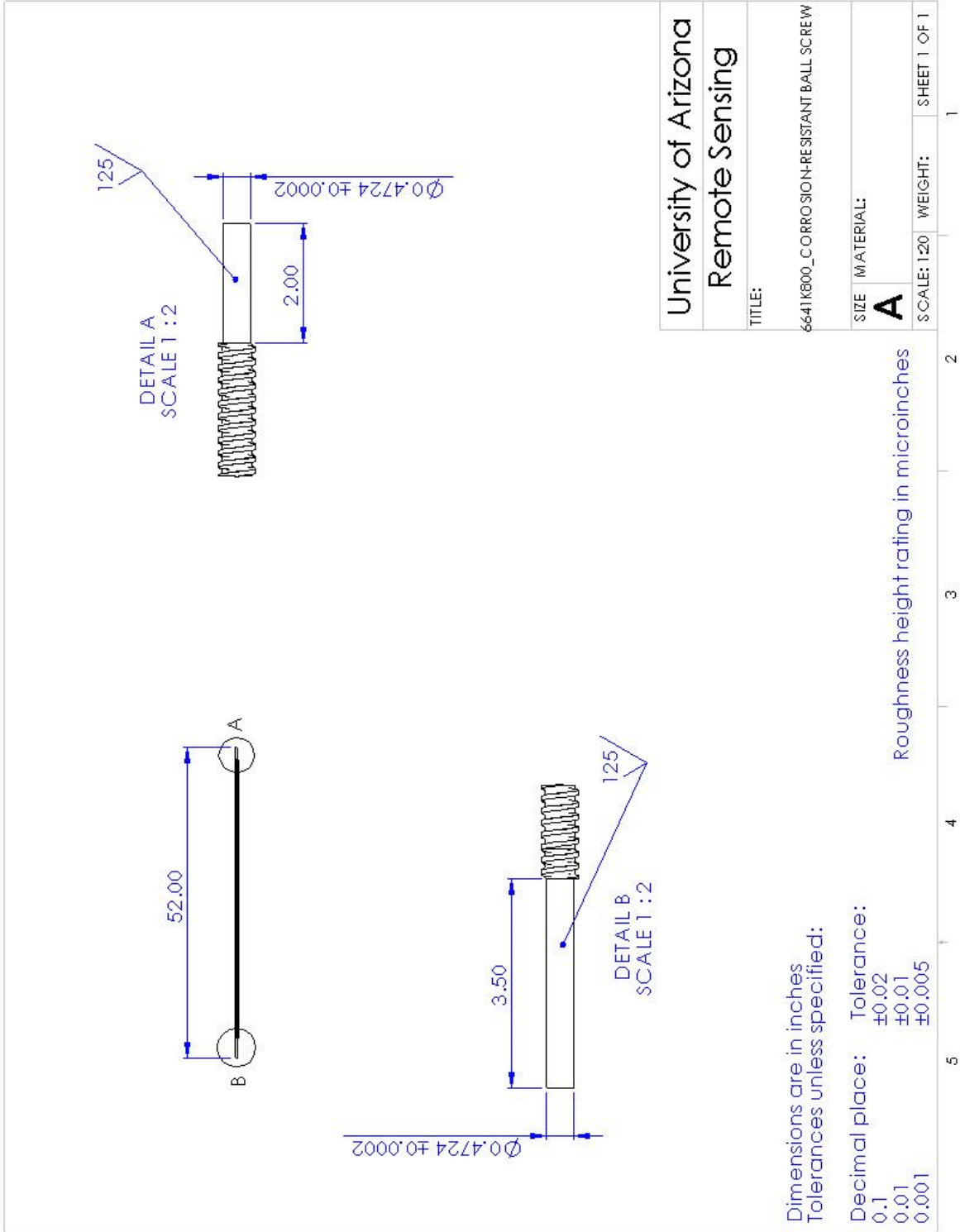




C.9 Ball Nut Bracket



C.10 Modified Ball Screw



References

- (1) Thome, K., Crowther, B. and Biggar, S. "Reflectance- and Irradiance-Based Calibration of Landsat-5 Thematic Mapper." *Canadian Journal of Remote Sensing*. 23(4), 309-317. (1997)
- (2) Kuester, M., et al. "Comparison of surface reflectance measurements from three ASD FieldSpec FR spectroradiometers and one ASD FieldSpec VNIR spectroradiometer." 2001. IGARSS 2001. Scanning the Present and Resolving the Future. Proceedings. IEEE 2001 International Geoscience and Remote Sensing Symposium. 1, 72-74. (2001)
- (3) Czapla-Myers, J., Thome, K. and Buchanan, J. "Implication of spatial uniformity on vicarious calibration using automated test sites." *Proc. SPIE 6677, Earth Observing Systems XII*, 66770U. (2007)
- (4) A. Berk, P. Conforti, R. Kennett, T. Perkins, F. Hawes, and J. van den Bosch, "MODTRAN6: a major upgrade of the MODTRAN radiative transfer code" *Proc. SPIE 9088, Algorithms and Technologies for Multispectral, Hyperspectral, and Ultraspectral Imagery XX*, 90880H (2014)
- (5) Czapla-Myers, J., et al. "The Ground-Based Absolute Radiometric Calibration of Landsat 8 OLI." *Remote Sensing*. 7(1), 600-626. (2015)
- (6) Thome, K., et al. "Vicarious Calibration of ASTER via the Reflectance-Based Approach." *IEEE Transactions on Geoscience and Remote Sensing*, 46(10), 3285-3295. (2008)
- (7) Thome, K. "Absolute radiometric calibration of Landsat 7 ETM+ using the reflectance-based method." *Remote Sensing of Environment*, 78(1-2), 27-38. (2001)
- (8) Thome, K., et al. "Ground-reference techniques for the absolute radiometric calibration of MODIS." *Proc. SPIE 4135, Earth Observing Systems V*. 51-60. (2000)
- (9) Scott, K., Thome, K. and Brownlee, M. "Evaluation of Railroad Valley Playa for use in vicarious calibration." *Proc. SPIE 2818, Multispectral Imaging for Terrestrial Applications*. (1996)
- (10) Anderson, N. and Czapla-Myers, J. "Ground viewing radiometer characterization, implementation and calibration applications: a summary after two years of field deployment." *Proc. SPIE 8866, Earth Observing Systems XVIII*, 88660N. (2013)
- (11) Anderson, N., et al. "Design and calibration of field deployable ground-viewing radiometers." *Applied Optics*, 52(2), 231-240. (2013)
- (12) Thome, K., Smith, N. and Scott, K. "Vicarious calibration of MODIS using Railroad Valley Playa." IGARSS 2001. Scanning the Present and Resolving the Future. *Proc. IEEE 2001 International Geoscience and Remote Sensing Symposium*. 3, 1209-1211. (2001)
- (13) Chander, G., et al. "Applications of Spectral Band Adjustment Factors (SBAF) for Cross-Calibration." *IEEE Transactions on Geoscience and Remote Sensing*, 51(3), 1267-1281. (2013)

- (14) Chander, G., Meyer, D. and Helder, D. "Cross calibration of the Landsat-7 ETM+ and EO-1 ALI sensor." *IEEE Transactions on Geoscience and Remote Sensing*, 42(12), 2821-2831. (2004)
- (15) Chander, G., et al. "Cross-calibration of the Terra MODIS, Landsat 7 ETM+ and EO-1 ALI sensors using near-simultaneous surface observation over the Railroad Valley Playa, Nevada, test site." *Proc. SPIE 6677, Earth Observing Systems XII*, 66770Y. (2007)
- (16) Mishra, N., et al. "Radiometric Cross Calibration of Landsat 8 Operational Land Imager (OLI) and Landsat 7 Enhanced Thematic Mapper Plus (ETM+)." *Remote Sensing*, 6(12), 12619-12638. (2014)
- (17) Teillet, P.M., et al. "Impacts of spectral band difference effects on radiometric cross-calibration between satellite sensors in the solar-reflective spectral domain." *Remote Sensing of Environment*, 110(3), 393-409. (2007)
- (18) Thome, K., Wenny, B., Anderson, N., McCorkel, J., Czaplak-Myers, J. and Biggar, S. "Ultra-portable field transfer radiometer for vicarious calibration of earth imaging sensors." *Metrologia*, 55(3), S104. (2018)
- (19) Anderson, N., et al. "Design of an ultra-portable field transfer radiometer supporting automated vicarious calibration." *Proc. SPIE 9607, Earth Observing Systems XX*, 960709. (2015)
- (20) Czaplak-Myers, J. and Anderson, N. "Post-launch radiometric validation of the GOES-16 Advanced Baseline Imager (ABI)." *Proc. SPIE 10785, Sensors, Systems, and Next-Generation Satellites XXII*, 107851F. (2018)
- (21) Helder, D., et al. "Recent surface reflectance measurement campaigns with emphasis on best practices, SI traceability and uncertainty estimation." *Metrologia*, 49(2), S21-S28. (2012)
- (22) Beer, F., et al. "Mechanics of Materials." 5th. Singapore: McGraw-Hill. (2009)
- (23) Collins, D. "How to calculate motor drive torque for ball screws." *Linear Motion Tips*. [Online] Design World, May 18, 2016. <https://www.linearmotiontips.com/calculate-motor-drive-torque-ball-screws/>.